Citation for final published version:

Aster, Callum, Inserra, Cosimo , Pastorello, Andrea, Anderson, Joseph P., Bauer, Franz E., Bostroem, K. Azalee, Chambers, Kenneth, Chen, Tong-Wan, Farah, Joseph R., Fraser, Morgan, Fugazza, Dino Pierluigi, Gromadzki, Mariusz, Gutiérrez, Claudia P., Howell, D. Andrew and et. al. 2026. SN 2024abvb: a Type Ibn/Icn supernova with evidence of helium and an extreme offset from its host galaxy. Monthly Notices of the Royal Astronomical Society , stag404. 10.1093/mnras/stag404

Publishers page: https://doi.org/10.1093/mnras/stag404

SN 2024abvb: a Type Ibn/Icn supernova with evidence of helium and an extreme offset from its host galaxy

Callum Aster[1]★, Cosimo Inserra[1], Andrea Pastorello[2], Joseph P Anderson[3], Franz Erik Bauer[4], K. Azalee Bostroem[5,6], Kenneth C. Chambers[7], Ting-Wan Chen[8], Joseph R. Farah[9,10], Morgan Fraser[11], Dino Pierluigi Fugazza[12], Mariusz Gromadzki[13], Claudia P. Gutiérrez[14,15], D. Andrew Howell[9,10], Erkki Kankare[16], Tom L. Killestein[17], Niilo Koivisto[16], Giorgos Leloudas[18], J. D. Lyman[17], Kyle Medler[7], Shane Moran[19], Tomás E. Müller-Bravo[20,21], Giuliano Pignata[4], Miika Pursiainen[17], Fabio Ragosta[22,23], Andrea Reguitti[2,12], Jesper Sollerman[24], Giorgio Valerin[2], Ben Warwick[17], David R. Young[25].

[1] *Cardiff Hub for Astrophysics Research and Technology, School of Physics & Astronomy, Cardiff University, Queens Buildings, The Parade, Cardiff, CF24 3AA, UK*
[2] *INAF-Osservatorio Astronomico di Padova, Vicolo dell'Osservatorio 5, 35122 Padova, Italy*
[3] *European Southern Observatory, Alonso de Córdova 3107, Vitacura, Casilla 19001, Santiago, Chile*
[4] *Instituto de Alta Investigación, Universidad de Tarapacá, Casilla 7D, Arica, 1010000, Chile*
[5] *Steward Observatory, University of Arizona, 933 North Cherry Avenue, Tucson, AZ 85721-0065, USA*
[6] *LSST-DA Catalyst Fellow*
[7] *Institute for Astronomy, University of Hawaii at Manoa, 2680 Woodlawn Dr., Hawaii, HI 96822, USA*
[8] *Graduate Institute of Astronomy, National Central University, 300 Jhongda Road, 32001 Jhongli, Taiwan*
[9] *Las Cumbres Observatory, 6740 Cortona Drive, Suite 102, Goleta, 93117-5575, CA, USA*
[10] *Department of Physics, University of California, Santa Barbara, 93106-9350, CA, USA*
[11] *School of Physics, University College Dublin, LMI Main Building, Beech Hill Road, Dublin 4, D04 P7W1*
[12] *INAF – Osservatorio Astronomico di Brera, Via E. Bianchi 46, I23807 Merate (LC), Italy*
[13] *Astronomical Observatory, University of Warsaw, Al. Ujazdowskie 4, 00-478 Warszawa, Poland*
[14] *Institut d'Estudis Espacials de Catalunya (IEEC), Edifici RDIT, Campus UPC, 08860 Castelldefels (Barcelona), Spain*
[15] *Institute of Space Sciences (ICE, CSIC), Campus UAB, Carrer de Can Magrans, s/n, E-08193 Barcelona, Spain*
[16] *Department of Physics and Astronomy, University of Turku, 20014 Turku, Finland*
[17] *Department of Physics, University of Warwick, Gibbet Hill Road, Coventry CV4 7AL, UK*
[18] *DTU Space, Department of Space Research and Space Technology, Technical University of Denmark, Elektrovej 327, 2800 Kgs. Lyngby, Denmark*
[19] *School of Physics and Astronomy, University of Leicester, University Road, Leicester LE1 7RH, UK*
[20] *School of Physics, Trinity College Dublin, The University of Dublin, Dublin 2, Ireland*
[21] *Instituto de Ciencias Exactas y Naturales (ICEN), Universidad Arturo Prat, Chile*
[22] *Dipartimento di Fisica 'Ettore Pancini', Universita' di Napoli Federico II, Via Cinthia 9, 80126 Naples, Italy*
[23] *INAF – Osservatorio Astronomico di Capodimonte, Via Moiariello 16, I-80131 Naples, Italy*
[24] *The Oskar Klein Centre, Department of Astronomy, Stockholm University, AlbaNova SE-10691, Stockholm, Sweden*
[25] *Astrophysics Research Centre, School of Mathematics and Physics, Queen's University Belfast, Belfast BT7 1NN, UK*

Accepted XXX. Received YYY; in original form ZZZ

ABSTRACT

We present spectroscopic and photometric observations and analysis of SN 2024abvb, a peculiar transitional Type Ibn/Icn supernova located at an unusually large projected distance from its host galaxy (21.5 kpc). SN 2024abvb displays an extended rise time in the g- and o-bands (10.1 and 10.6 days respectively), followed by a linear decline in all photometric bands. Comparisons with other supernova subclasses show that the photometric and spectroscopic evolution of SN 2024abvb are distinct from Type Ibn and Type Icn events, with a higher peak r-band luminosity and lower blackbody temperatures. Spectra reveal an initial blue continuum and narrow P-Cygni profiles, with C ɪɪ λ5890 dominating in emission, persisting at late phases, and showing a rapid decline in the expansion velocity. Weak He ɪ λ5876 features are tentatively detected at early times. Analysis of progenitor scenarios rules out thermonuclear origins based on incompatible light curve shapes and spectral signatures. A rare massive star progenitor appears unlikely given the low local star formation rate. The most plausible origin is an ultra-stripped supernova scenario involving a binary system; this best explains the observed separation from the host, the low circumstellar material mass, the fast photometric evolution and the low nickel production, although a discrepancy in model versus observed ejecta mass remains. These results reinforce the classification of SN 2024abvb as a distinctive Type Ibn/Icn event and highlight the diversity of progenitor channels for interacting supernovae.

Key words: transients: supernovae – supernovae: individual: SN 2024abvb

1 INTRODUCTION

Massive stars, those with an initial mass at the Zero Age Main Sequence exceeding roughly 8 $M_{\odot}$, end their lives as core-collapse supernovae (CCSNe). Observationally, CCSNe divide into hydrogen-rich (Type II) and hydrogen-poor (Type I) classes based on the presence or absence of Balmer lines in their spectra (Minkowski 1941; Filippenko 1997). This spectroscopic dichotomy reflects fundamentally different pre-explosion evolutionary pathways, driven by mass-loss processes.

Hydrogen-poor SNe (Type I) can arise when strong stellar winds or eruptive episodes remove the progenitor's hydrogen envelope. In isolated massive stars, radiatively driven winds become increasingly efficient at higher metallicity and luminosity, eventually peeling away the outer layers to reveal helium- and heavier-element cores (Kudritzki & Puls 2000). Such progenitors give rise to "stripped-envelope" supernovae (SE SNe), subdivided into Type Ib (helium lines present), Type IIb (hydrogen mostly stripped) and Type Ic (helium lines weak or absent) events (Woosley et al. 1995). Binary interactions, through Roche-lobe overflow or common-envelope ejection, can produce analogous stripping even for stars whose winds alone would not suffice (e.g. Smith et al. 2011).

Wolf–Rayet (WR) stars, characterised by their broad emission-line spectra, constitute one of the possible SE SN progenitors (Sukhbold et al. 2016). Within the WR family, nitrogen-rich (WN) stars are generally linked to Type Ib explosions, whereas carbon-rich (WC and WO) stars correspond to Type Ic events (Wheeler & Levreault 1985; Hunter et al. 2009). However, lower-mass helium stars, produced via binary mass transfer, may also explode as SE SNe (e.g. Drout et al. 2014; Lyman et al. 2016; Prentice et al. 2018), complicating the mapping between spectral subtype and progenitor mass (Eldridge et al. 2013).

When significant amounts of circumstellar material (CSM) remain close to the progenitor at collapse, either retained from previous eruptions or not fully dispersed by winds, the SN ejecta can collide with this CSM. The interaction converts kinetic energy into radiation, and the observed SN show multi-component emission profiles generated by the ejecta and the CSM. These interacting SNe are spectroscopically classified as Type IIn (hydrogen-rich CSM), Type Ibn (helium-rich CSM; Pastorello et al. 2007; Foley et al. 2007), Type Icn (carbon-rich CSM; Gal-Yam et al. 2022) or Type Ien (silicon- and sulfur-rich CSM; Schulze et al. 2025). Type Ibn SNe exhibit strong, narrow He I lines and generally lack the oxygen and carbon signatures that characterize Type Icn events, whereas Type Icn SNe show prominent O II-III and C II-III lines alongside P-Cygni profiles at early times (Pellegrino et al. 2022). The recently identified class of Type Ien shows a lack of CNO but strong Si and S narrow emission lines (Schulze et al. 2025). SN 2019hgp was the first firm Type Icn classification (Gal-Yam et al. 2022) and has been followed by an additional four confirmed events: one reclassification (SN 2019jc; Pellegrino et al. 2022) and three new discoveries (SNe 2021ckj, 2021csp, 2022ann; Nagao et al. 2023; Davis et al. 2023; Perley et al. 2022). These events share uniform characteristics: spectral line velocities of $\sim 10^3$–10^4 km s^{-1}, consistent with WR progenitor winds; rise times to peak light of ~ 7 days; peak absolute magnitudes clustered around $M_r \approx -19$ mag; spectra dominated by narrow C and O emission/absorption, indicative of recently ejected carbon-rich CSM. The features shared among Type Icn events, fast rise time and the presence of carbon, might indicate similar progenitor scenarios. However, other photometric and spectroscopic properties suggest a wider diversity in progenitor scenarios. These scenarios range from carbon-rich, hydrogen- and helium-depleted stars that underwent a major mass-loss episode shortly before core collapse to compact objects in binary systems.

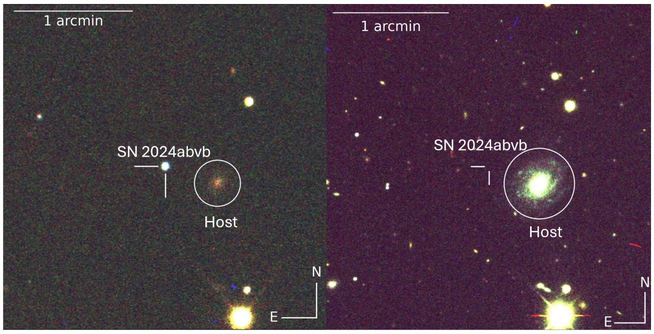

Figure 1. Left Panel: *gri* image stack from Las Cumbres Observatory (LCO) data (taken on 2024/11/28) with SN and host labelled. A 1 arcmin scale bar has been plotted at the top left of the image, with north oriented up and east to the left. **Right Panel:** *gri* image stack from Dark Energy Spectroscopic Instrument (DESI) Legacy Imaging Surveys (LIS, Dey et al. 2019) data (taken on 2019/08/08), all markers are the same across both images. Although we see clear spiral arms in the LIS image, the SN position is offset from the host.

Here, we present the evolution of SN 2024abvb (see also Hu et al. 2026; INTEL Collaboration 2026; Shi et al. 2026), a new member of the SN Ibn/Icn family. SN 2024abvb was discovered by the Asteroid Terrestrial-impact Last Alert System (ATLAS; Tonry et al. 2018) on 22 November 2024 (MJD 60636.36, Tonry et al. 2024), and subsequently classified as a Type Icn at $z = 0.039$ by the NUTS collaboration (MJD 60641.90, Stritzinger et al. 2024). Due to the tentative detection of helium, we reconsider this classification. Type Icn SN are classified based on the absence of helium in their spectra. Thus, the tentative detection of helium in the medium-resolution spectra differs from a pure Type Icn event classification, suggesting that a transitional classification is more appropriate. Here we present ultraviolet (UV) through near-infrared (NIR) photometry alongside optical spectroscopy, with systematic comparisons to previously reported Type Icn, Type Ibn and transitional objects of Type Ibn/Icn. Throughout the paper we assume a standard ΛCDM cosmology (Komatsu et al. 2011) with $\Omega_M = 0.27$, $\Omega_\Lambda = 0.73$ and $H_0 = 70 \mathrm{km\,s^{-1} Mpc^{-1}}$ which gives D_L =172.2 Mpc.

SN 2024abvb is spatially offset from its probable host galaxy (host $z = 0.039$), therefore host extinction is likely negligible. We adopt the line-of-sight extinction measurement at the SN position, $A_V = 0.507$ mag, corresponding to $E(B-V)_{\mathrm{MW}} = 0.164$ mag (Schlafly & Finkbeiner 2011), as our total extinction. Figure 1 shows a composite Las Cumbres Observatory (LCO) *gri* image of the SN field ~6 days post explosion together with that of the Legacy Imaging Survey (DR10) showing the host. Relevant SN and host information can be found in Table 1.

The structure of this paper is as follows. Section 2 describes the discovery, follow-up strategy and data reduction procedures for both photometry and spectroscopy. In Section 3 we present the detailed analysis of the light curves and spectral series. In Section 4 we discuss the host of SN 2024abvb and provide an analysis of its environment. Section 5 we combine our findings and discuss the implications for the progenitor system and circumstellar environment of SN 2024abvb. Finally, in Section 6 we summarise the paper and make conclusions.

2 DATA

2.1 Photometry

Our photometric monitoring of SN 2024abvb utilises a heterogeneous suite of facilities and filter systems to achieve broad wavelength coverage (see Table A2). Optical imaging in the Johnson–Cousins B- and V-bands and an Sloan Digital Sky Survey (SDSS)-like r-band was obtained with the Andalucia Faint Object Spectrograph and Camera (ALFOSC) on the Nordic Optical Telescope (NOT; Djupvik & Andersen 2010). Complementary V-band frames were secured using the ESO Faint Object Spectrograph and Camera (EFOSC2) mounted on the New Technology Telescope (NTT; Buzzoni et al. 1984). Additional optical data in the SDSS-like g, r, i and z filters were acquired with the 1m network of telescopes of the Las Cumbres Observatory (LCO; Brown et al. 2013), utilising the Sinistro cameras. Since instruments with very different passbands were used for the follow-up of SN 2024abvb we checked the uncertainties of passband corrections (e.g., Stritzinger et al. 2002; Pignata et al. 2004) to standardise photometry to a common system. We used the S3 package (Inserra et al. 2018) and found that such correction is an order of magnitude lower than the telescope photometric uncertainties. Imaging was taken with the Rapid Eye Mount (REM) telescope (Covino et al. 2002). The Near–infrared (NIR) imaging in the J-, H- and K-bands were taken with the REMIR instrument. Optical V-, R- and I- frames were taken with the ROS2 instrument. Data from the Gravitational-wave Optical Transient Observer (GOTO; Steeghs et al. 2022a) were obtained as part of regular all-sky surveying. Image reduction and calibration was performed in real-time using the GOTO transient pipeline. Forced aperture photometry at the position of SN 2024abvb was performed to recover the final GOTO light curve.

All CCD data were processed within the IRAF[1] environment. Standard reduction steps including overscan correction, bias subtraction, flat-fielding and trimming were applied, and SN photometry was extracted via point-spread function fitting on the final reduced frames.

Ultraviolet observations were obtained with the Neil Gehrels *Swift* Observatory's Ultraviolet/Optical Telescope (UVOT; PI: Farias) through the $uvw2$, $uvm2$, $uvw1$, u, b and v filters. These data were calibrated to the Vega system and reprocessed independently using a custom pipeline based on the HEASARC software suite.

To further supplement our proprietary measurements, we incorporated archival photometry from several time-domain surveys. These include the Zwicky Transient Facility (ZTF; g, r filters; Bellm et al. 2019), Pan-STARRS1 (w filter; Chambers et al. 2019), the BlackGEM array (q filter; Groot et al. 2024), the Gravitational-wave Optical Transient Observer (GOTO; L filter; Steeghs et al. 2022b; Dyer et al. 2024) and the ATLAS survey (cyan and orange filters; Jedicke et al. 2012). Non-public Pan-STARRS1 measurements were obtained under prior collaboration agreements. Final magnitude measurements from these surveys were retrieved using their data pipelines (Magnier 2006; Magnier et al. 2020).

2.2 Spectroscopy

Nine epochs of spectroscopic data were acquired with the EFOSC2 instrument mounted on the ESO New Technology Telescope (NTT) as part of the ePESSTO+ collaboration. We obtained low-resolution spectra using grisms 11 and 16, while medium-resolution observations were secured with grism 18 (see Table A1 for the full observation log, including wavelength coverage and resolving powers). The raw frames were processed and calibrated using the Public ESO Spectroscopic Survey of Transient Objects (PESSTO) pipeline[2] (Smartt et al. 2015), which performs bias subtraction, flat-field correction, wavelength calibration and flux calibration in a uniform and reproducible manner. All ePESSTO+ spectra will be available through the ESO Science Archive Facility as standard phase 3 ESO products. All spectra are available on WISeREP[3] (Yaron & Gal-Yam 2012).

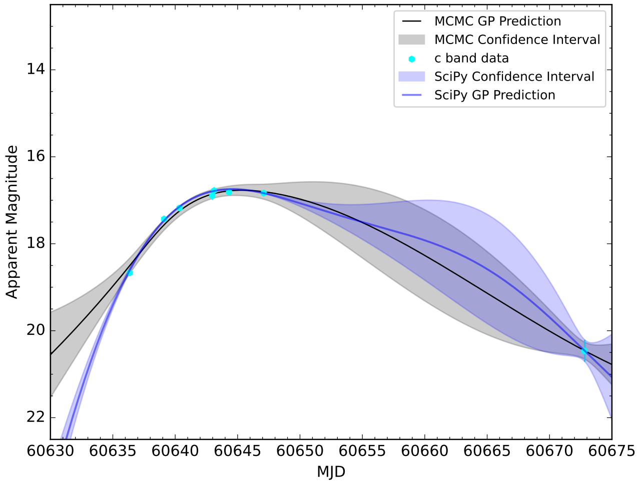

Figure 2. The SciPy and emcee optimised fit for the c-band data

Table 1. Key information for the SN and host. Time of last non-detection is 60634.5 MJD in the o-band. We adopt the line-of-sight extinction measurement $E(B-V) = 0.164$, at the SN position (Schlafly & Finkbeiner 2011). No evident reddening is observed in the host (e.g. no narrow absorption lines). Hence, the MW reddening is the total.

Time of First Detection (MJD)	60636.62
Estimated Time of Explosion (MJD)	60635.45 ± 1.1
Estimated Time of Maximum (MJD)	60645.13 ± 0.4
RA (J2000)	01:10:57.53
Dec (J2000)	-05:44:07.91
Redshift	0.039
$E(B-V)_{\mathrm{MW}}$ [mag]	0.164
m_V^{peak} (mag)	16.70
M_V^{peak} (mag)	−19.43
$t_{\mathrm{rise,g/C}}$ (days)	10.1
$t_{1/2,\mathrm{decline,g/C}}$ (days)	7.6
Separation from host (arcmin)	0.464
Separation from host (kpc)	21.5

3 CHARACTERISING SN 2024ABVB IN THE CONTEXT OF INTERACTING SUPERNOVAE

In this section, we compare photometry and spectra of SN 2024abvb to other SNe, chosen based on the fact that are well sampled and

---

[1] The Image Reduction and Analysis Facility (IRAF) is distributed by the National Optical Astronomy Observatory, operated by AURA under cooperative agreement with the National Science Foundation.

[2] https://github.com/svalenti/pessto

[3] https://www.wiserep.org

studied SNe. The chosen comparison Type Icn are reported above in Section 1 while the others are: SN 2010al (Type Ibn, Pastorello et al. 2015); SN 2023emq (Type Ibn/Icn, Pursiainen et al. 2023) and iPTF14aki (Type Ibn, Hosseinzadeh et al. 2017).

3.1 Light curve

To determine the epoch of maximum light, we first fitted the ATLAS c-band light curve, chosen for its dense temporal sampling from first detection through peak, using a 1D Gaussian process (GP) regression implemented in the GEORGE package (Ambikasaran et al. 2015) with an exponential-squared kernel. Initial kernel hyperparameters were optimised via SCIPY minimisation, after which we employed the EMCEE Markov Chain Monte Carlo (MCMC) sampler (Foreman-Mackey et al. 2013) to sample from the posterior distribution of the GP model parameters. The MCMC-refined GP fit closely matches the initial optimisation. For completeness, we also applied an analogous GP fit to the bolometric light curve, retrieving a similar result. From these analyses, we adopt MJD 60645.13 ± 0.4 as the time of maximum light (defined as epoch 0). The explosion epoch was estimated as the midpoint between the first w-band detection and the preceding o-band non-detection at 0.3 mag deeper, yielding MJD 60635.45 ± 1.1.

Using the MCMC-optimised GP model, we computed rise times from explosion to maximum light and 20-day decline rates in each filter. The rise time, $t_{\rm rise}$, is defined as the interval between the explosion epoch and the GP-determined peak MJD. Decline rates (Δm_{20}) were measured as the difference in magnitude between peak and 20 days post-peak. In the V-band we find $\Delta m_{20} = 2.6 \pm 0.3$ mag, whereas in the i-band $\Delta m_{20} = 1.1 \pm 0.3$ mag. The slower decline in redder bands is not unusual in CCSNe and even more so in interacting SNe, as it suggests reprocessing of high-energy (X-ray/UV) photons into optical wavelengths (e.g. Chevalier & Fransson 1994).

Figure 3 displays the UV–NIR light curves of SN 2024abvb. The g-band rise time of 10.1 ± 0.3 days is notably longer than the $\lesssim 5.2$ day values typical of other Type Icn events (Table 2, Pellegrino et al. 2022; Perley et al. 2022; Nagao et al. 2023). Similarly, the ATLAS o-band rise time of 10.5 ± 0.4 days slightly exceeds the ~ 8 days measured for SN 2022ann (Davis et al. 2023). Across all bands, we observe approximately linear declines in magnitude, with the steepest fades in the UV and blue optical filters and the gentlest in the NIR.

In Figure 4 we compare the r-band light curve of SN 2024abvb with those of well-sampled interacting SNe in the same time frame of SN 2024abvb: SNe 2019hgp (Type Icn), 2022ann (Type Icn) and 2010al (Type Ibn). SN 2024abvb reaches peak r-band light ($M_r \approx -19.4$) at 12.1 ± 0.3 days and shows a $\Delta m_{20}(r) = 1.6 \pm 0.3$ mag. For reference, SN 2019hgp exhibits a similar $\Delta m_{20}(r) = 1.6 \pm 0.2$ mag but peaks at a lower luminosity ($M_r \approx -18.6$), whereas the prototypical Type Ibn SN 2010al fades more slowly, with $\Delta m_{20}(r) = 1.4 \pm 0.2$ mag. SN 2022ann displays a two-stage decline: an initial slow phase (~ 0.2 mag per 20 days) followed by a rapid drop (~ 2.0 mag per 20 days), indicative of interaction with a denser CSM. SN 2019hgp has a low-mass CSM environment (0.2 $M_\odot$, Gal-Yam et al. 2022). Assuming SN 2024abvb light curve is dominated by the CSM interaction, the similarity of its decline to that of SN 2019hgp could suggest a comparable low-mass CSM environment for SN 2024abvb and progenitor scenario. However, SN 2024abvb also has a higher peak luminosity compared to SN 2019hgp ($M_r \approx -19.2$ mag), consistent with a somewhat more efficient radiative conversion (Chevalier & Fransson 2017).

Table 2. Comparison of rise-times and half decline rates in the g-band for SN 2024abvb and all Type Icn SNe where they were measurable. We see that the g-band rise time for SN 2024abvb is much higher than for other Type Icn SNe, while the half decline rate is comparable.

SN	Rise Time (days)	Half decline rate (days)
2024abvb	10.1 ± 0.3	7.6 ± 0.3
2019jc	3.2 ± 0.1 [a]	3.1 ± 0.1 [a]
2019hgp	5.2 ± 0.2 [a]	8.0 ± 0.2 [a]
2021csp	1.8−4.0 [b]	9.1 ± 0.8 [b]
2021ckj	3.3 ± 0.2 [c]	4.7 ± 0.2 [c]

a Pellegrino et al. (2022)
b Perley et al. (2022)
c Nagao et al. (2023)

3.2 Bolometric light curve

Bolometric luminosities were derived by first converting the extinction-corrected broadband magnitudes (Section 3.1) into monochromatic fluxes at each filter's effective wavelength. A spectral energy distribution (SED) was then assembled over the observed wavelength range, and the integrated flux, $F_{\rm bol}$, was computed under the assumption of negligible contribution beyond the integration limits. Luminosities were obtained via

$$L_{\rm bol} = 4\pi D^2 F_{\rm bol},$$

where D is the previously determined distance to SN 2024abvb (Section 1).

Pseudo-bolometric points were initially calculated for epochs with concurrent coverage in at least four optical bands; for epochs with fewer than four filters, missing fluxes were estimated by low-order ($n \leq 3$) polynomial interpolation of adjacent light-curve data. When interpolation was not possible, magnitudes were extrapolated by assuming constant colours between the nearest epochs.

The resulting bolometric light curve (Figure 5) reaches a peak luminosity of $\log(L_{\rm bol}/{\rm erg\,s^{-1}}) = 43.7$ in approximately 10 days, followed by a nearly linear decline over the subsequent ~ 30 days. In the second panel of Figure 5, we show the black-body temperature, $T_{\rm BB}$, inferred from SED fits. $T_{\rm BB}$ attains a maximum of roughly 14000 K, remains on a quasi-plateau, then decreases rapidly before settling at around 6400 K around 20 days post-peak. These temperatures are substantially lower than those reported for SNe 2022ann and 2019hgp, which peaked near 25000 K and 30000 K, respectively.

The third panel of Figure 5 presents the photospheric radius

$$R_{\rm ph} = \sqrt{\frac{L_{\rm bol}}{4\pi\sigma T_{\rm eff}^4}},$$

where σ is the Stefan–Boltzmann constant. $R_{\rm ph}$ increases to a maximum of $\sim 2.1 \times 10^{15}$ cm at ~ 6 days after peak, then declines slowly and plateaus at $\sim 0.65 \times 10^{15}$ cm by ~ 25 days post-peak. Overall, the estimated radius of SN 2024abvb is larger than that showcased by SN 2019hgp, but at a size not unusual for SNe (e.g. Kasen & Woosley 2009; Dessart et al. 2022; Chiba & Moriya 2024).

The bottom panel of Figure 5 shows the fractional flux contributions from the ultraviolet (UV), optical and near-infrared (NIR) regimes. Initially, the UV accounts for $\sim 53\%$ of $F_{\rm bol}$ and the optical for $\sim 29\%$, with the NIR contributing $\sim 17\%$. Over the first two days post-maximum, the optical fraction rises to match the UV at $\sim 43\%$, consistent with high-energy photon reprocessing by circumstellar material (CSM). The NIR fraction decreases to $\sim 12\%$

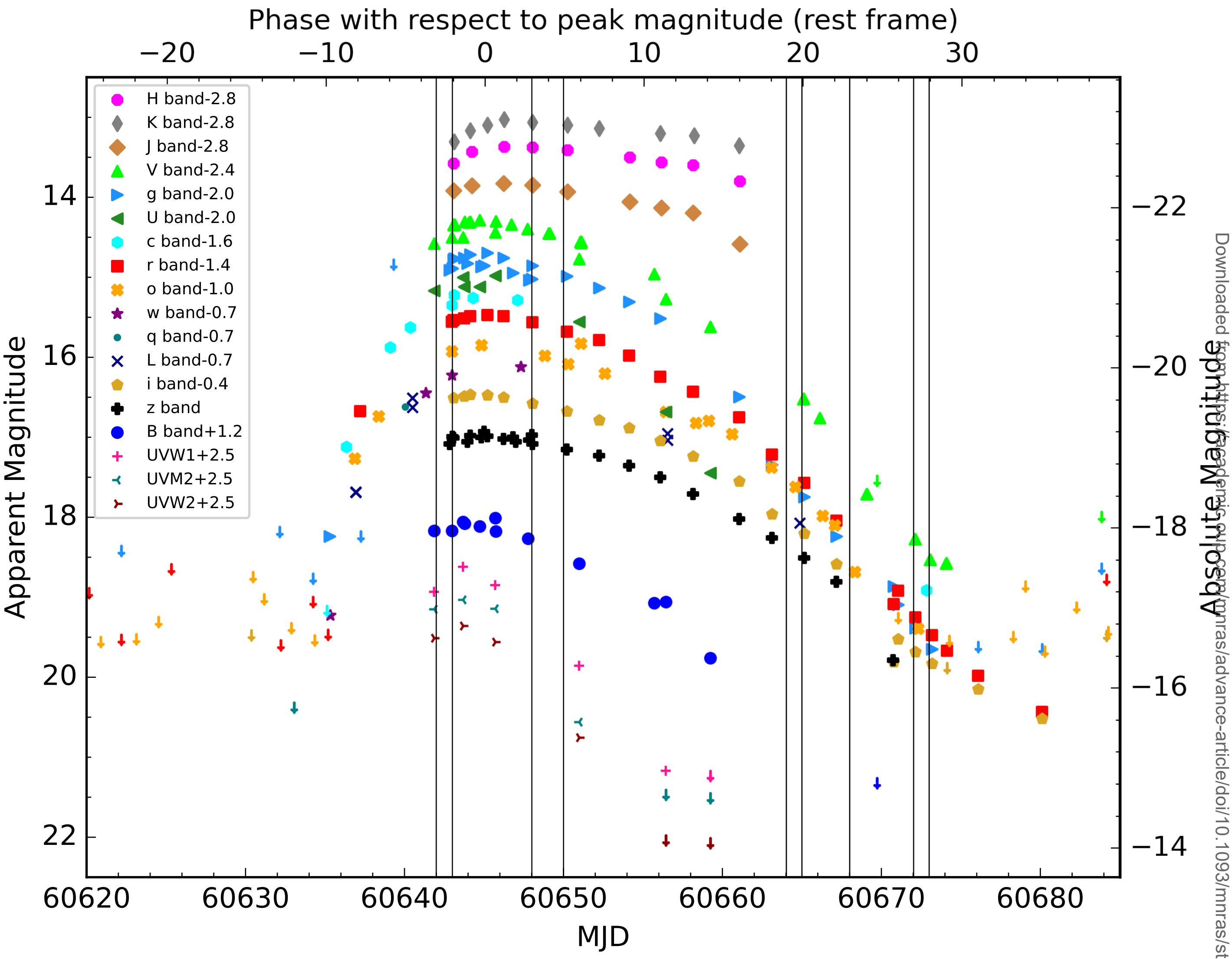

Figure 3. Light curves of SN 2024abvb from AFOSC, ATLAS, Pan-STARRS, LCO, NTT, Swift, NOT, ZTF, REM, TTT, Moravian, BlackGem and GOTO for all available bands from the UV-NIR. The phase is given relative to the V-band maximum. The legend indicates which shape and colour is associated with specific bands. Non-detections are shown with downward arrows. The rise times and decline rates for each band can be seen in Table 2. The vertical black lines indicate the epochs when spectra were taken. The L- and q-bands refer to GOTO and BlackGem bands, respectively. The figure is not extinction corrected. $griz$ are AB magnitudes, as are those of the surveys ATLAS, PS1 and GOTO. $UBVJHK$ are Vega magnitudes.

in the early decline, then increases slightly as the optical component plateaus, ultimately stabilising just above its initial level. Within our measurement uncertainties, the NIR contribution remains effectively constant, implying that any dust formation either is minimal or occurs at epochs later than our final NIR observations (Mattila et al. 2008).

3.3 Spectral evolution and line measurements

Figure 6 displays the spectral evolution of SN 2024abvb, spanning from three days before maximum light to approximately one month thereafter. Prominent transitions of C ii and O ii are marked alongside the tentative detections of H i , He i and He ii. The continua are consistent with the photospheric temperatures derived from our black-body fits.

To quantify the kinematic and flux properties of individual lines, we fitted Gaussian profiles using the Lmfit package[4] (Newville et al. 2014). For the C ii $\lambda5890$ feature, a composite model comprising a central Lorentzian (narrow emission) plus a broader Gaussian component was employed to capture both the line core and extended wings.

In the four low-resolution spectra obtained near peak brightness, the continuum is blue and several narrow P-Cygni profiles are evident, with C ii $\lambda5890$ dominating in emission. At early epochs (0–4 days relative to peak), this line exhibits a full width at half maximum (FWHM) of ~ 41 Å, corresponding to a velocity of $\sim 2100\,\mathrm{km\,s^{-1}}$, and an integrated flux of 1.0×10^{-16} erg s^{-1} cm^{-2}. By 6 days post-peak, the FWHM decreases to ~ 32 Å (velocity $\sim 1600\,\mathrm{km\,s^{-1}}$) with

---

[4] Lmfit is a non-linear least-squares minimisation and curve-fitting library for Python.

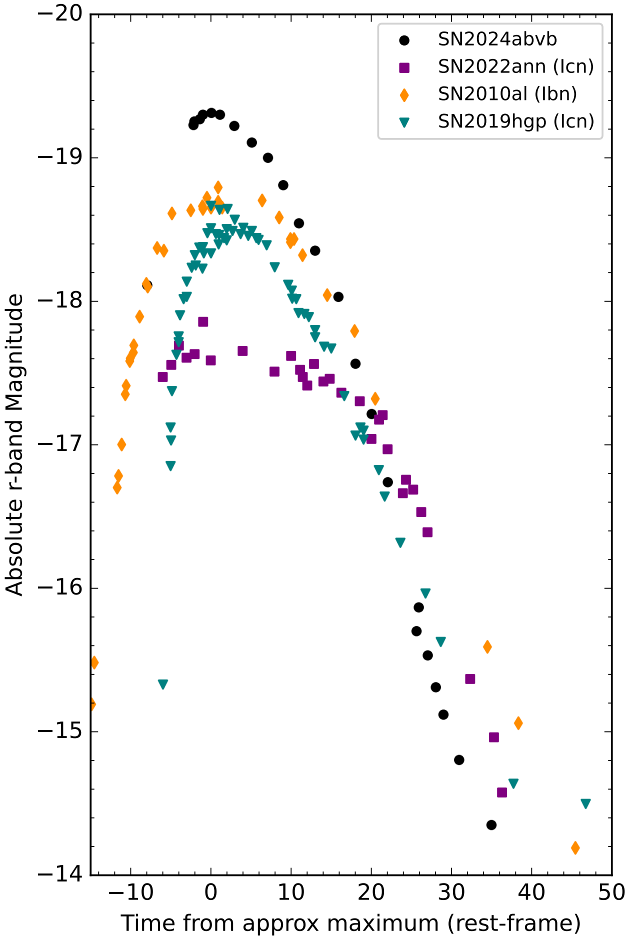

Figure 4. Comparison photometry in the r-band (absolute magnitude) for SN 2024abvb, the Type Ibn (SN 2010al; Pastorello et al. 2015) and two other Type Icn (SNe 2022ann and 2019hgp; Davis et al. 2023).

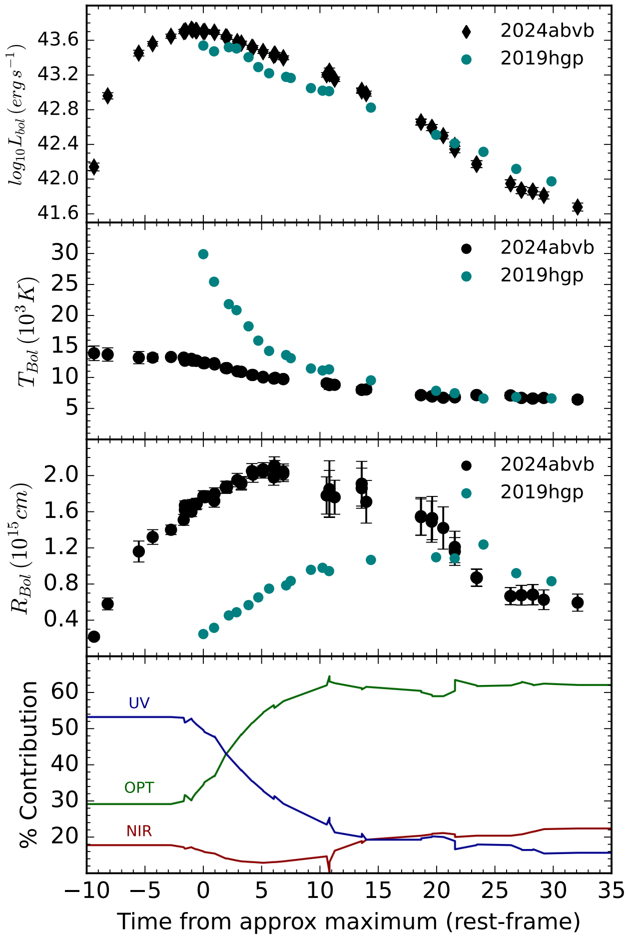

Figure 5. The top panel shows the bolometric light curve. The second panel shows the estimated temperature derived from the black-body fits. The third panel shows the photospheric radius. The bottom panel shows the contribution of each part of the electromagnetic spectrum over time (UV: $uvw2$, $uvm2$, $uvw1$. Optical: u, B, g, V, c, r, o, i, z. NIR: J, H, K). Each panel, besides the last, shows a comparison between SNe 2024abvb and 2019hgp (Gal-Yam et al. 2022). SN 2019hgp is the closest photometric analogue, therefore we use this for comparison.

a flux of 8.8×10^{-17} erg s^{-1} cm^{-2}. Beyond 20 days, the continuum flattens, likely due to metal-line blanketing below 4700 Å, and C ɪɪ λ5890 evolves into a P-Cygni profile with FWHM ~ 28 Å (velocity ~ 1400 km s^{-1}) and flux 2.5×10^{-17} erg s^{-1} cm^{-2}.

Medium-resolution spectra (grism #18 at the NTT+EFOSC2; Table A1) enable a detailed view of the 4600–6500 Å region (Figure 7). Here, C ɪɪ λ5890 has FWHM 32.7 Å (velocity ~ 1600 km s^{-1}) and flux 1.5×10^{-16} erg s^{-1} cm^{-2} at peak, evolving to FWHM 29.1 Å (velocity ~ 1400 km s^{-1}) and flux 7.6×10^{-17} erg s^{-1} cm^{-2} by +6 days. And at ~ 30 days FWHM 16.8 Å (velocity ~ 800 km s^{-1}) and flux 2.88×10^{-17} erg s^{-1} cm^{-2}. All FWHM measurements are above our spectra resolution (see Table A1). A weaker feature at ~ 5876 Å, present until +4 days, is consistent with being He ɪ λ5876. The red wing of C ɪɪ λ5890 exhibits a broad shoulder which, as mentioned above, can be due to metal-line blanketing in the blue part or suggestive of asymmetric CSM.

O ɪɪ λ4651 is detected in low-resolution spectra prior to +20 days, with an early FWHM of 9.3 Å (flux 1.2×10^{-16} erg s^{-1} cm^{-2}) broadening to 26.0 Å (flux 9.4×10^{-17} erg s^{-1} cm^{-2}) by +6 days; it is absent at later epochs. In contrast, C ɪɪ λ5890 persists, switching to a P-Cygni morphology in both low- and medium-resolution spectra after +20 days (FWHM 19.4–27.8 Å, flux ~ 4.0×10^{-17} erg s^{-1} cm^{-2}).

Additional features, including H ɪ λ4861, O ɪɪ λ4651 and Fe ɪɪ λ5363, are discernible in medium-resolution data, with clear P-Cygni profiles persisting at late times.

3.4 Spectral comparison with other Type Ibn, Type Icn and transitional events

Figure 8 displays the EFOSC2 spectra of SN 2024abvb at epochs near maximum light and approximately one month later, compared with those of SNe 2018fmt, 2019jc, 2021csp, 2023emq (Pursiainen et al. 2023), iPTF14aki and 2022ann. Comparison SNe were chosen based on having spectra covering from peak epoch to roughly a month later in their evolution. The sample includes well studied Type Ibn events (SNe 2018fmt and iPTF14aki), canonical Type Icn events (SNe 2019jc and 2021csp) and recognised transitional Type Ibn/Icn objects (SN 2023emq), chosen to assess whether SN 2024abvb exhibits intermediate characteristics.

At early times, SN 2024abvb exhibits a notably blue continuum, closely matching the continua of SNe 2021csp and 2023emq, remain-

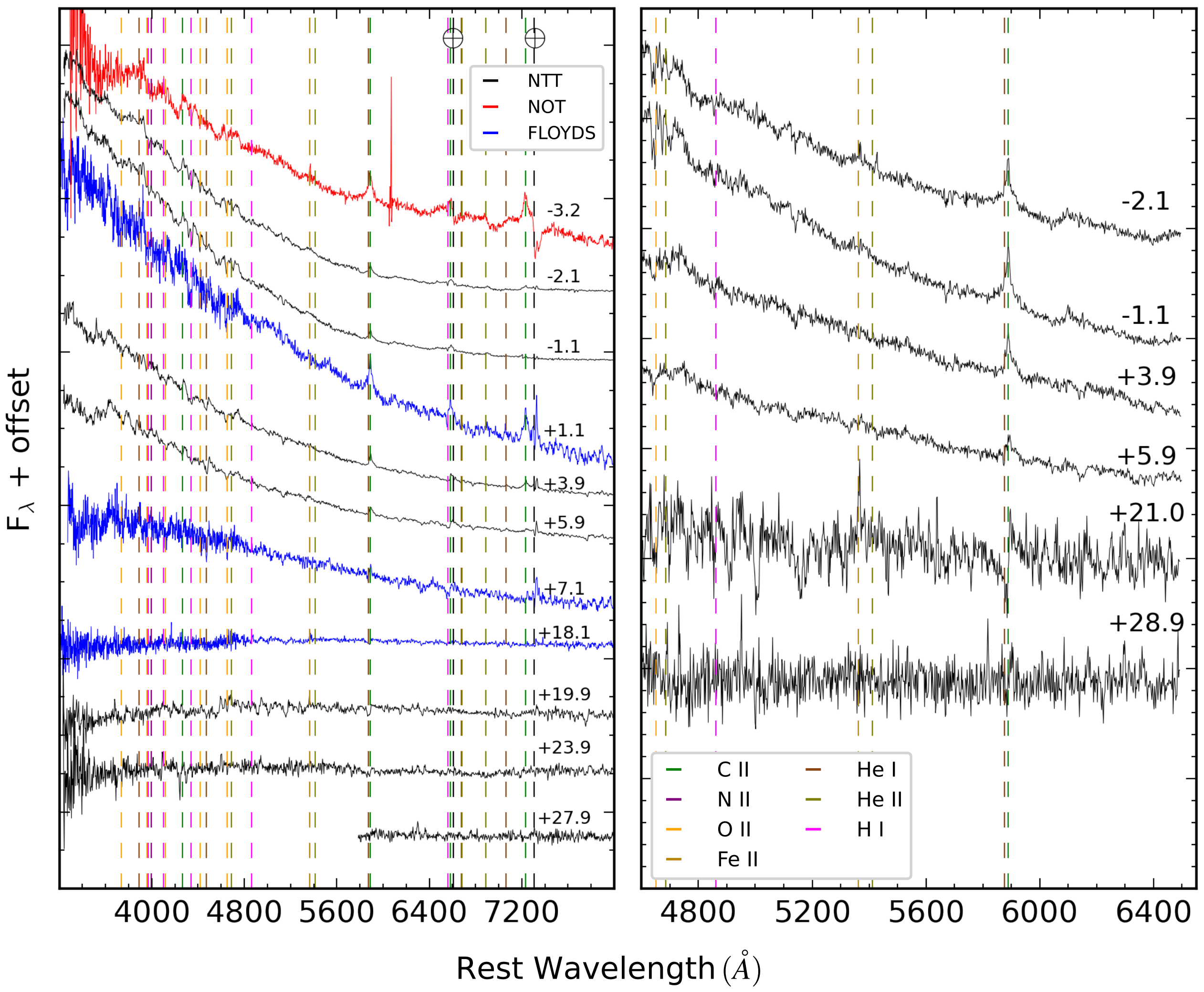

Figure 6. Left panel: All low-resolution spectra (see Table A1), corrected for redshift and reddening, for SN 2024abvb taken between −3.23 days and 27.90 days relative to V-band maximum brightness. The C ii, H i, He i, He ii, O ii, N ii and Fe ii lines are marked. We see some telluric contamination; however, it leaves the spectral lines mostly unaffected. The cross in this figure shows the telluric lines. **Right panel:** All medium resolution spectra (see Table A1), corrected for redshift and reddening, for SN 2024abvb taken between −2.05 days and 28.90 days relative to V-band maximum brightness. In all instances, multi-component decomposition was fully resolved, as were the subsequent P-Cygni profiles.

ing bluer than those of the other Type Ibn and Type Icn comparisons. The persistence of this blue slope, also evident in the minimal B-band decline of $\Delta m(B) \approx 0.16$ mag between the first and third spectra, suggests more efficient conversion of high-energy (X-ray/UV) photons into optical wavelengths than in typical Type Icn events. We note that this is at odds with what is observed in the temperature evolution. In contrast, SNe 2019jc and 2021csp display a pseudo-continuum dominated by blended emission lines (e.g. Gal-Yam et al. 2022), which is not apparent in SN 2024abvb. Although Figure 8 hints at a weak pseudo-continuum between 4600 and 6000 Å in SN 2024abvb, this feature remains ambiguous.

In the bottom panels of Figure 8, SN 2019hgp, the closest photometric analogue to SN 2024abvb, exhibits broader and faster line profiles and displays intermediate-mass element features such as Mg i, which are absent in SN 2024abvb. Moreover, oxygen emission lines in SN 2019hgp are considerably stronger, and its late-time spectrum develops the characteristic iron pseudo-continuum common to many Type Icn (and interacting) events. SN 2021csp, similarly to SN 2019hgp, shows an Fe pseudo-continuum but otherwise shows very few emission or absorption features. SN 2022ann shows a much flatter continuum than the other three Type Icn presented, but similar to SN 2021csp it shows very few prominent absorption and emission features. This is in stark contrast to SNe 2024abvb and 2019hgp, which both display prominent features in pure emission. The one transitional SN Type Ibn/Icn we present shows an interesting blueward feature, similar to that of SN 2024abvb; however, on further inspection, this is more likely due to an Fe pseudo-continuum as seen in other Type Icn SNe. Such a continuum seems lacking in SN 2024abvb where we see a sharp decrease at $\sim$4500 Å, implying this feature is formed through an alternative mechanism. We observe that iPTF14aki shows a flatter continuum with characteristically broad Helium lines typically seen in late-time Type Ibn spectra (Hosseinzadeh et al. 2017). This, along with the other features noted in SN 2024abvb, gives strong evidence that SN 2024abvb is inconsistent with a Type Ibn SN classification.

The close temporal comparison reveals that SN 2019hgp has el-

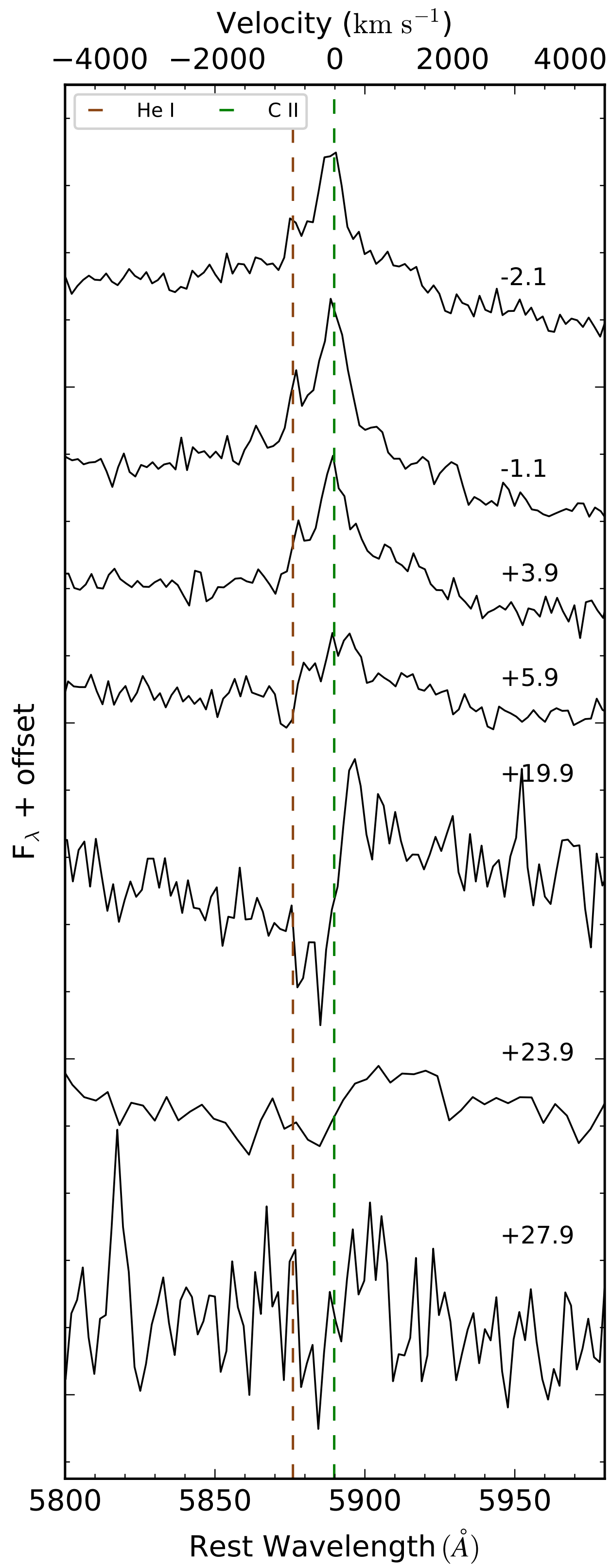

Figure 7. The same spectra are shown here as in Figure 6; however, this is a zoom-in on the most prominent spectral feature, C II λ5890 Å, with medium resolution spectra (see Table A1).

evated flux compared to SN 2024abvb, both blueward of 4600 Å and redward of 6200 Å, whereas between these wavelengths (4600–6200 Å) the fluxes of the two SNe are broadly comparable, with both displaying a flux enhancement near 6000 Å. These differences reinforce the classification of SN 2024abvb as a transitional Type Icn/Ibn object with a relatively low-mass, carbon-rich CSM.

3.5 Expansion velocities of the CSM

We derived the expansion velocity of the carbon-rich CSM from C II λ5890. For epochs up to ∼10 days after maximum light, we measured the full width at half maximum (FWHM) of the Gaussian fits, while at later times we determined velocities from the minima of the P-Cygni absorption troughs. The resulting velocity evolution is plotted in Figure 9. Differences between low- and medium-resolution measurements are attributable to instrumental resolving power.

As mentioned above, He I λ5876 is also present and alters the overall profile of the C II line, as such we use our medium resolution spectra measurements as a more accurate diagnostic. At early epochs, the C II line exhibits velocities of $\sim 1500\,\mathrm{km\,s^{-1}}$, declining smoothly to $\sim 800\,\mathrm{km\ s^{-1}}$ by the final measurement. This smooth decline is observed in both the low- and medium-resolution spectra, with $\Delta V_{20-\mathrm{low}} \sim 660 \pm 150\,\mathrm{km\,s^{-1}}$ and $\Delta V_{20-\mathrm{med}} \sim 490 \pm 100\,\mathrm{km\,s^{-1}}$, respectively. In both cases, the minimum measured values remain above the instrumental resolution (460 km s^{-1} for gr18 and 870 km s^{-1} for gr11), although the final velocity point in the medium-resolution data lies close to this threshold. The final measurement conflicts with early WC and canonical WO wind speeds of $> 1000\,\mathrm{km\,s^{-1}}$ (Sander et al. 2019; Smith & Aller 1971). However, canonical wind speeds for WN and late type WC9 stars are lower at $v_\mathrm{wind} > 650\,\mathrm{km\ s^{-1}}$ and $\sim 450\,\mathrm{km\ s^{-1}}$, respectively (Hamann et al. 2019; Smith & Aller 1971). This suggests that the CSM may have been produced by a discrete eruption, by binary interaction, by a WN star in a binary system or by a WC9 star with emission transitioning from lower density CSM (higher velocity lines) to higher density inner regions (lower velocity lines). In the eruptive scenario, the required mass-loss rate would be sufficiently high to dominate the circumstellar density, whereas a sustained WR wind alone would be less likely to generate the observed density profile; this interpretation is in line with Smith (2017).

Comparable velocities have been reported for other interacting SNe. For example, SN 2019hgp displayed C III λ4650 velocities in excess of $1500\,\mathrm{km\ s^{-1}}$, consistent with WR progenitors but quoted as a lower limit due to spectral resolution (Gal-Yam et al. 2022). Conversely, SN 2022ann exhibited expansion speeds of $\sim 800\,\mathrm{km\ s^{-1}}$. Davis et al. (2023) favour a binary scenario given the line driven wind speeds are below early WC and WO wind speeds (Sander et al. 2019). The close agreement between the velocity of SN 2022ann and our late-time measurement for SN 2024abvb supports a binary progenitor system and is therefore inconsistent with a single early WC or WO star progenitor. This suggests that the progenitor scenario is either a WN star, a late type WC9 star or more complex than a single WR star.

4 HOST ANALYSIS

From optical images, SN 2024abvb appeared to be far from any potential host and possibly hostless, with the nearest galaxy located 0.464 arcmin (21.5 kpc) S/W of the SN (Figure 1). To determine whether the S/W galaxy is the host, we obtained a combination of Gr11 and Gr16 spectra. The slit was centered on the nucleus and

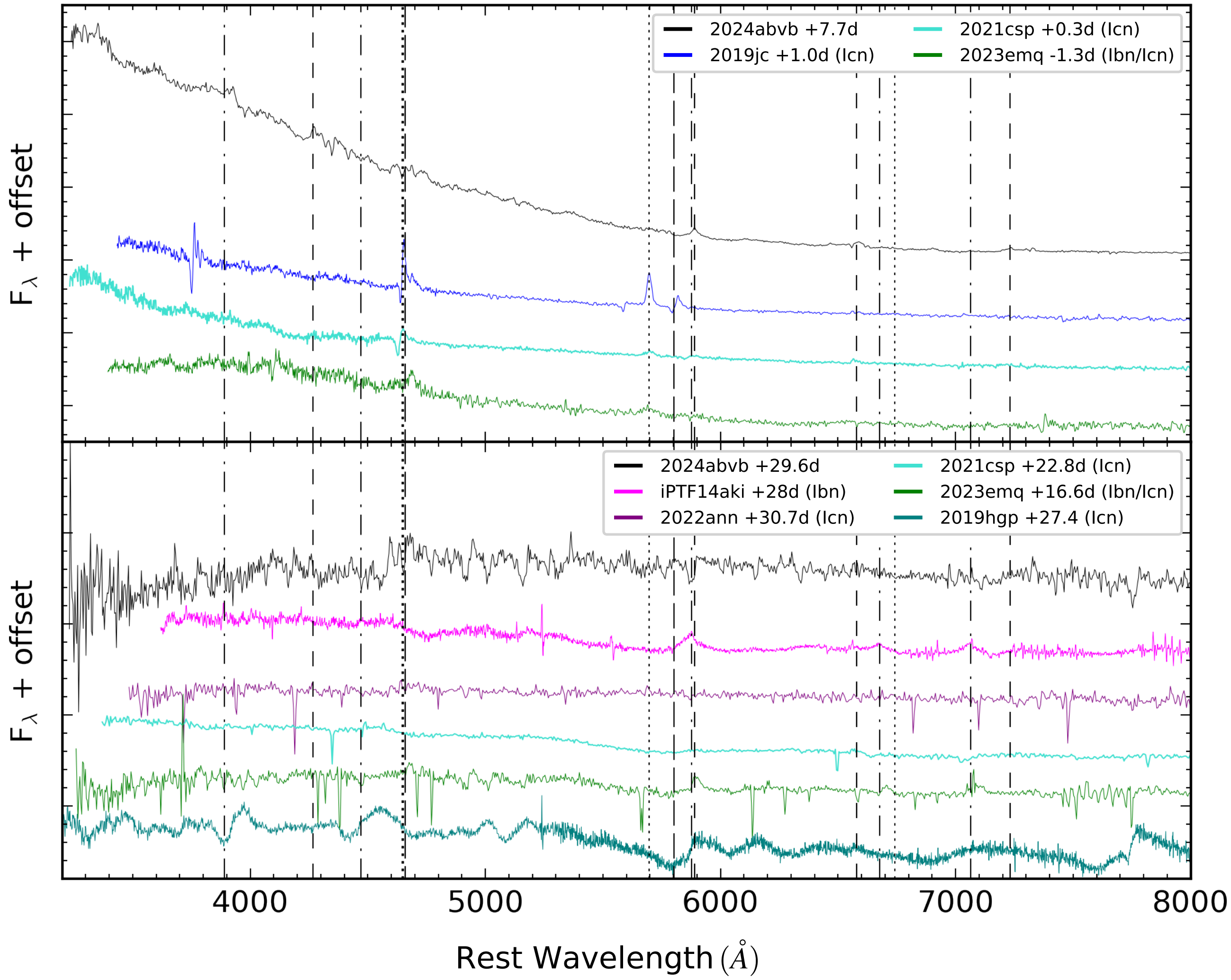

Figure 8. SN 2024abvb spectra compared to other Type Ibn, Type Icn and transitional Type Ibn/Icn SNe. Both panel have dashed lines to depict different elements: C II - - - ; C III ·········; C IV —— ; He I —·—· ; **Top panel:** Early time (~ 8 days) spectra comparison for SN 2024abvb, SN 2018fmt, SN 2019jc, SN 2021csp and SN 2023emq. The specific colours and phase times for each SN are shown in the legend. The phase is with respect to the explosion time as we did not have access to photometric data for the comparison SNe. **Bottom panel:** Late time (~ 29 days) spectra comparison for SN 2024abvb, SN 2021csp, iPTF14aki, SN 2022ann, SN 2023emq and SN 2019hgp.

covered the majority of the host. This translates to a mostly global spectra but was only used for determining the redshift.

Unfortunately, due to environmental conditions, the Gr11 spectrum had S/N ≤ 3 and was therefore unusable. The Gr16 spectrum (upper panel of Figure 10) also has low S/N, however, features were visible. A redshift of $z = 0.039$, the same value as identified for SN 2024abvb through spectral comparison, appears to confirm this galaxy as the likely host, as Hα is detected at the corresponding wavelength.

To retrieve the host galaxy properties, *griz* and mid-infrared Wide-field Infrared Survey Explorer (WISE) $W1$, $W2$ & $W3$ magnitudes were taken from the Dark Energy Spectroscopic Instrument (DESI) Legacy Imaging Surveys (LIS, Dey et al. 2019), Data Release 10. The $W4$ was also available but was excluded as that is sensitive to AGN dust emission and we do not implement for such a correction in our simple models, meaning $W4$ would have a poor fit. We also include *JHKs* data from the Vista Hemisphere Survey Data Release 7 (VHS DR7), this survey uses the Visible and Infrared Survey Telescope for Astronomy (VISTA) telescope (Emerson et al. 2006) using the VISTA infrared camera (Dalton et al. 2006). The LIS data were then input into PROSPECTOR[5] (Johnson et al. 2021) to estimate the host parameters such as stellar mass and star formation rate (SFR). We used the following Prospector parameters: Star formation history is a delayed Tau model; Inital mass function (IMF) is the Chaubrier IMF model (Chabrier 2003); dust type is a MW extinction model (Cardelli et al. 1989); $\log(Z/Z_\odot)$ and age are uniform functions; $\log(\tau)$ and $\log(M/M_\odot)$ are log uniform functions.

The bottom panel of Figure 10 presents a best-fit model for *grizy*, *JHKs*, and $W1$-$W3$ bands given by PROSPECTOR. The model provides useful insight into the galaxy's parameters, and has a $\chi^2 = 0.025$ whcih is mainly driven by the optical bands that have lower uncertainties than the near and mid infrared ones. We note that NIR

---

[5] PROSPECTOR is a package to conduct principled inference of stellar population properties from photometric and/or spectroscopic data using flexible models.

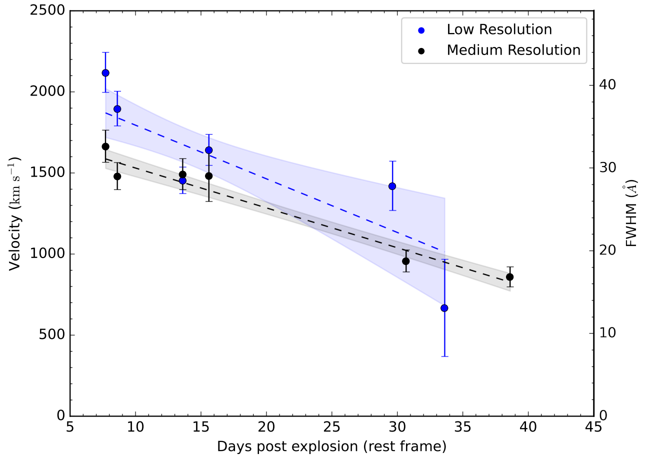

Figure 9. C II 5890 Å comparison velocities for low and medium resolution spectra. The first four epochs were measured using the emission component FWHM, while the remaining two were measured from P-Cygni minima. The dashed line depicts the best-fit while the shaded regions display the 1σ confidence intervals.

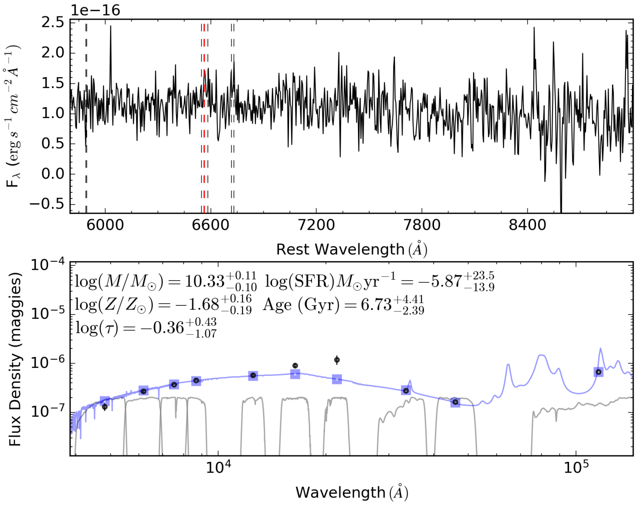

Figure 10. Top panel: Host spectrum with galaxy lines (Hα indicated in red, Na I, N II and S II are indicated in black) at the assumed redshift of $z = 0.039$. **Bottom panel:** Best fit SED obtained from PROSPECTOR. The black points are the LIS $griz$, $W1$,$W2$ and $W3$ and VHS $JHKs$ data points with error bars. The blue boxes and line are the fitted SED and data points. This fit has a reduced $\chi^2 = 0.025$.

flux is sensitive to intermediate-age stars (0.5–2 Gyr), also known as Thermally-Pulsing AGB (TP-AGB) stars, and differences of 0.5 dex in JHK from stellar population synthesis models have been widely reported (Conroy et al. 2009). This difference is enhanced by the choice of a parametric star formation history (SFH). The Prospector model outputs are $\log(M/M_\odot) = 10.33^{+0.11}_{-0.10}$, $\log(Z/Z_\odot) = -1.68^{+0.16}_{-0.19}$, $\log(\tau) = -0.36^{+0.43}_{-1.07}$, Age (Gyr) $= 6.73^{+4.41}_{-2.39}$, $\log(\mathrm{SFR})M_\odot\mathrm{yr}^{-1} = -5.87^{+23.5}_{-13.9}$ and presented in the bottom panel of Figure 10. The results imply a host galaxy of low mass, slightly above the dwarf galaxy range (Geha et al. 2012), and well below larger galaxies such as the Milky Way ($\sim 10^{12} M_\odot$, Watkins et al. 2019). These galaxies tend to have a lower metallicity and age Gallazzi et al. (2005). This is consistent with our results and suggests that the host is likely a young, low-mass, and low-metallicity galaxy. However, because a parametric SFH was adopted, these results should be interpreted as indicative rather than definitive, since a non-parametric SFH would provide a more robust constraint. The peak SFR occurs a $t_{\mathrm{peak}} = \tau \sim 0.28$ Gyr, suggesting that SFR was very high at early time and then decreased, which is consistent with old stellar population. However, such a result mathematically forces the instantaneous SFR at the present epoch to be close to zero ($\sim 10^{-6}$). Because delayed-τ models enforce a monotonic decline in star formation, we caution from over-interpreting the instantaneous SFR derived from this parameterisation.

The separation of SN 2024abvb from its presumed host also appears atypical compared to other Type Icn SNe, which are all located within their host galaxies (Gal-Yam et al. 2022; Pellegrino et al. 2022; Davis et al. 2023; Perley et al. 2022; Nagao et al. 2023). However, there are known Type Ibn SNe such as, PS1-12sk (Hosseinzadeh et al. 2019), with a large host separation (28.1 kpc). Due to the large separation, we investigate the possibility that SN 2024abvb is hosted by a dwarf satellite galaxy that is gravitationally bound to the host, similarly to the Small Magellanic Cloud (SMC). LIS deep imaging reports depths of $m_g = 25.08$, $m_r = 25.41$, $m_i = 26.86$ and $m_z = 23.33$. Doliva-Dolinsky et al. (2025) find that NGC3109, an SMC-like dwarf galaxy has $M_V \sim 14.9$. This can be roughly converted to g via $g = V + 0.60(B - V) - 0.12$ where $(B - V) \sim 0.5$ (Sharina 2019). This gives $M_g \sim -15.1$ which when converted to riz gives: $M_r \sim -15.0$, $M_i \sim -14.9$ and $M_z \sim -14.8$ which correspond to $m_g \sim 21.08$, $m_r \sim 21.18$, $m_i \sim 21.28$ and $m_z \sim 21.38$ at D_L =172.2 Mpc (the SN and host distance). Thus, if a SMC like satellite was the host of SN 2024abvb, we would have detected it within the deep LIS imaging, effectively ruling out this possibility.

5 DISCUSSION

SN 2024abvb appears to be a peculiar event for several reasons: its offset from the host galaxy is atypical for its class (21.5 kpc); it shows C II λ5890 and He I λ5876 in the spectra, with a velocity decrease from ~1500 km s^{-1} to ~800 km s^{-1}; the unusually low ionization state of carbon or any other CNO element; a blackbody temperature up to a factor of two lower than that of other interacting Type Ibn/Icn SNe during the first month of evolution.

The spectroscopic and photometric evolution of SN 2024abvb clearly indicates the presence of a dense CSM surrounding the progenitor. From the blackbody fit to the SED (see Section 3.2) and the bolometric luminosity, the peak radius is 2.1×10^{15} cm, approximately 10^3 times larger than that of a WR star (Hainich et al. 2014), suggesting that the CSM is not gravitationally bound to the star. Following the formalism of Smith & McCray (2007), the peak luminosity (L_{max}) produced by the ejecta–CSM shock scales with the CSM shell mass, the pseudo-photospheric velocity (v_{ph}), and the rise time (t_{max}). Using v_{ph} = 1500 km s^{-1} (Section 3.5), t_{max} = 10.1 d (Section 3.1), and $L_{\mathrm{max}} = 2.9 \times 10^{43}$ erg s^{-1} (Section 3.2), we infer a CSM mass of roughly 1.7 $M_\odot$. Assuming a single-progenitor scenario, the aforementioned radius and a constant CSM velocity of 1500 km s^{-1}, consistent with carbon-rich WR winds, the mass loss would have begun approximately 0.5 yr before the explosion. However, this would imply an enormous mass-loss rate ($\sim 3.4 \mathrm{M}_\odot$ yr^{-1}), which has never been observed/derived for a WR. As a consequence, it is unlikely that the progenitor scenario involves a single WR star losing mass via wind.

To reproduce the bolometric light curve of SN 2024abvb under

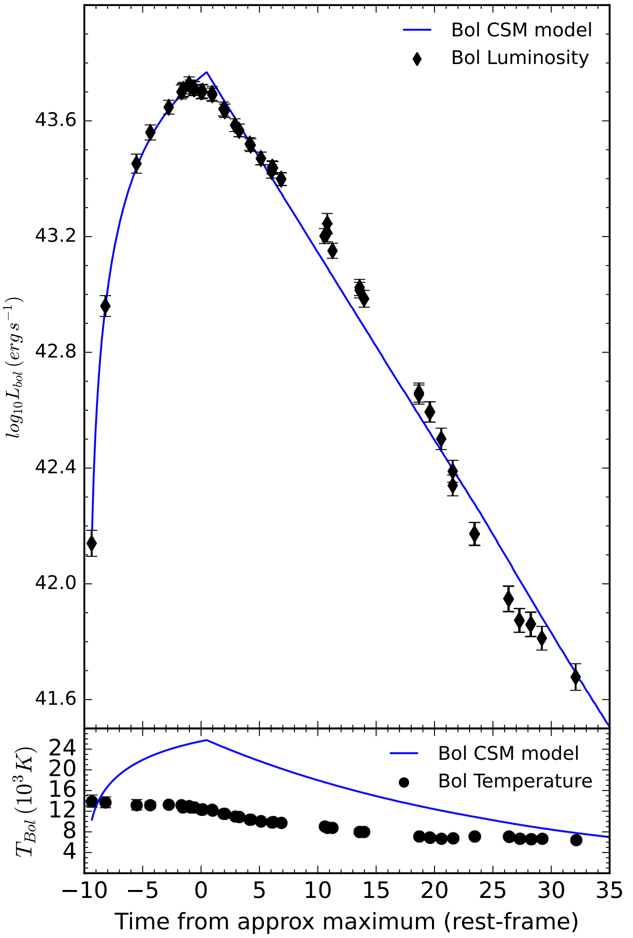

Figure 11. Bolometric light curves with CSM modelling. **Top Panel:** Bolometric light curves with a bolometric CSM model. We see a good fit (χ^2 = 4.16) of this model with our bolometric data. **Bottom Panel:** Blackbody derived temperature and the CSM model.

these assumptions, we employed a semi-analytical model based on Chatzopoulos & Wheeler (2012). We investigated both shell and wind CSM configurations, finding that the shell model provides a better overall fit (lower χ^2). We allowed for a contribution from ^{56}Ni to the luminosity. The inner and outer power-law slopes of the SN ejecta density profile were fixed to $\delta = 2$ and $n = 9$, respectively. We adopted Thomson scattering as the dominant opacity source and assumed a helium-poor composition, giving $\kappa = 0.10$ cm^2 g^{-1}. We allowed for Ni^{56} to contribute to the bolometric light curve fitting, but found that the best fit models required no Ni^{56} contribution. Our best-fitting model, shown in the top panel of Figure 11, yields the following parameters: $M_{\rm ej} = 3.9$ M$_\odot$, $M_{\rm csm} = 0.49$ M$_\odot$ and KE = 0.3×10^{51} erg. The model reproduces the bolometric light curve relatively well ($\chi^2 = 4.16$). The retrieved system properties point to a relatively low CSM mass, consistent with the photometric comparison in Figure 4. The absence of Ni^{56} suggests that the luminosity is dominated by ejecta–CSM interaction rather than radioactive heating. Additionally, we used the MOSFiT[6] (The Modular

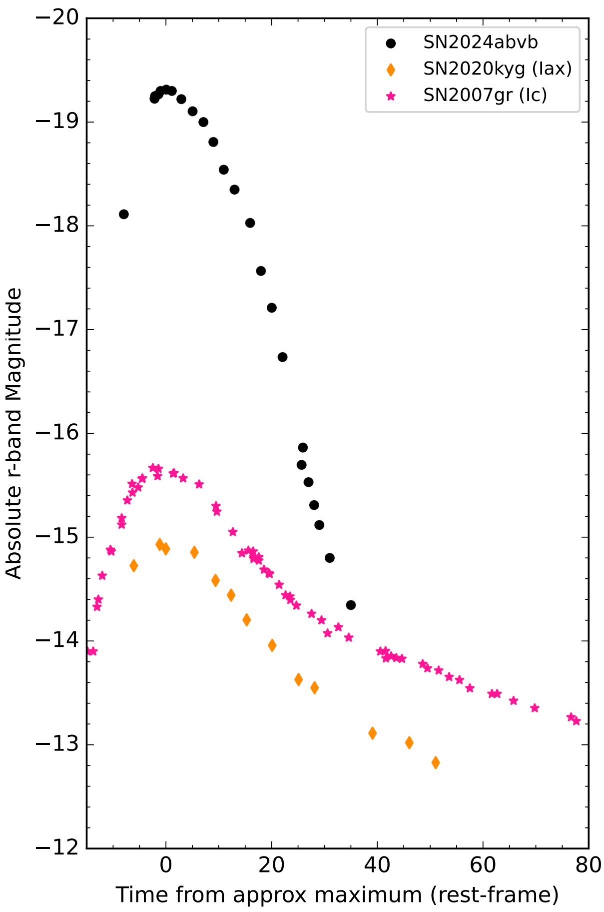

Figure 12. Comparison photometry in the r-band for SN 2024abvb, a Type Iax SN (2020kyg, Srivastav et al. 2022) and a Type Ic SN (2007gr, Hunter et al. 2009).

Open Source Fitter for Transients) Python package to fit the bolometric light curve and its uncertainties. The model assumed a Type Ic SN with a CSM contribution and $\kappa = 0.10$ cm^2 g^{-1}. The best fit (Figure A1 and A2) returned a $M_{csm} = 0.21$ M$_\odot$ and a $M_{ej} = 0.43$ M$_\odot$ albeit with a much higher $\chi^2_{reduced} = 175.2$ than the above semi-analytical model despite using the same formalism of Chatzopoulos & Wheeler (2012).

Figure 11 (bottom panel) shows a significant discrepancy between the temperature derived from blackbody fits and that predicted by the best-fitting CSM model. The temperature evolution for SN 2024abvb is also low when compared to SN 2019hgp (Figure 5), indicating that SN 2024abvb exhibits intrinsically lower temperatures than other interacting Type Ibn/Icn SNe.

The large projected distance of SN 2024abvb from its presumed host suggests two possible explanations. It could have been a long-lived star that was dynamically ejected (Perets 2008; Irrgang et al. 2018; Jordan et al. 2012). Alternatively, it is possible for local high-SFR to be present within a low-SFR galaxy (Vázquez-Semadeni et al. 2009), thus a short-lived progenitor that formed in situ is also possible. Because the spectra are dominated by CSM-interaction

---

[6] MOSFiT is a Python package for fitting and estimating the parameters of transients via user-contributed transient models.

signatures, the underlying SN cannot be directly constrained spectroscopically.

For Completeness, before discussing the most compelling scenarios, we briefly address the possibility of a Type Ia SN being the underlying cause of SN 2024abvb. Type Iax events are substantially less luminous than Type Ia SNe (McCully et al. 2014), and are the only thermonuclear event with a lower luminosity than SN 2024abvb at all epochs. In Type Iax events, carbon typically appears in absorption (Foley et al. 2013) rather than emission, implying relatively cool material far from the progenitor system. Type Iax SNe can exhibit carbon in their spectra, as their progenitors are C/O white dwarfs and some carbon may remain unburned during the explosion (Jha et al. 2006). This is inconsistent with the dense, carbon-rich CSM located in close proximity to the progenitor inferred for SN 2024abvb. Finally, merger events between two white dwarfs, particularly ONe+CO mergers as discussed by Wu et al. (2024), remain a plausible channel. Such mergers can produce bolometric light curves resembling those of Type Icn SNe such as SN 2019jc and SN 2021csp, and therefore could potentially explain SN 2024abvb. However, such a scenario should lead to an event somehow similar to SN 2005E (Perets et al. 2010) exhibiting calcium-rich spectral features. If SN 2024abvb arose from a similar channel we would likewise expect calcium lines to be present. The absence of calcium features in the spectra of SN 2024abvb does not obviously support this progenitor scenario.

5.1 SN 2024abvb as a rare massive star in a region with a very low star formation rate

Figure 12 demonstrates that it is, in principle, possible to obscure a Type Ic SN beneath the light curve of SN 2024abvb. The initial velocity of the C II λ5890 line, ~1500 km s^{-1}, is compatible with typical WR wind speeds. However, the subsequent decrease in velocity is difficult to explain in a scenario where the CSM is created by a constant wind, as unshocked wind material should not decelerate on the observed timescale (e.g. Sander et al. 2019; Hamann et al. 2019). It is worth mentioning that a decrease in WR wind speed has been observed in WC9 stars, and explained via a line emission region transitioning from outer, lower density regions, to higher density regions, resulting in lower line velocities (Smith & Aller 1971). However, such interpretation would not explain the weak He I, as WC9 stars typically show strong He I in their spectra, roughly equivalent to C II in intensity (Torres & Conti 1984). This behaviour instead suggests that the CSM may have been intrinsically slower and that we never observed the unshocked component. Under this interpretation, a single-star progenitor pathway becomes unlikely given the inferred velocities. A binary scenario (Crowther 2007b, e.g.) where one of the stars is a WR, by contrast, remains plausible as it naturally accommodates substantial mass stripping, as well as significant mass loss shortly before explosion. This is broadly consistent with the order-of-magnitude estimates discussed above (see Section 5).

The isolated position of the progenitor could be explained through several channels. One possibility is that the star was a hypervelocity object (>800 km s^{-1}, Perets 2008) ejected from the host galaxy following an interaction with either the central supermassive black hole (SMBH) or an intermediate-mass black hole (IMBH) (Perets 2008; Irrgang et al. 2018). Alternatively, the star may have experienced an asymmetric eruptive event that imparted a substantial kick (a few hundred km s^{-1}), displacing it from its natal environment (Jordan et al. 2012). Although such eruptions are commonly associated with Type Ia progenitors, an asymmetric outburst remains a viable mechanism for a massive star. Assuming that the massive star was ejected through the hypervelocity channel (Perets 2008, ~ 800 km s^{-1}), and given a projected offset of 21.5 kpc, the travel time required to reach the explosion site is ~ 26.3 Myr. This is much longer than the expected lifetimes of massive stars, which are ~ 5 Myr (Meynet & Maeder 2005; Crowther 2007a), rendering this scenario highly unlikely. The minimum projected separation between the SN position and the outermost spiral arm of the host galaxy is ~ 10.72 kpc (0.231 arcmin), corresponding to a travel time of ~ 13.1 Myr which is still more than twice the typical lifetime of stars in this mass range. Furthermore, Eldridge et al. (2011) argue that core-collapse SNe are unlikely to originate from progenitors located more than ~ 100 pc from their birth sites.

Finally, it is possible, albeit rare, that the progenitor simply formed at its current location.

5.2 SN 2024abvb as an ultra-stripped supernova

Ultra-stripped SNe (USSNe, Tauris et al. 2013) arise in binary systems composed of a compact object and a helium star. Such a configuration allows the system to be dynamically ejected from its host while still providing sufficient time for the helium star to evolve and explode as the observed SN. USSNe proceed through two main channels: iron core-collapse SNe (Fe CCSNe, Tauris et al. 2017) and electron-capture SNe (EC SNe, Nomoto 1987). While Fe CCSNe are essentially conventional core-collapse explosions of compact helium stars, EC SNe occur when the helium core collapses directly to a neutron star due to the loss of electron degeneracy pressure, triggered by electron captures in an ONeMg core. This collapse then produces a thermonuclear-like explosion (Tauris et al. 2017).

The USSNe scenario naturally explains the presence of CSM. Binary stripping can deposit material in the immediate vicinity of the system with velocities lower than those expected for single WR-star winds. In such cases, stripping of the helium star exposes a nearly bare metal core, potentially accounting for the higher-order elements present in the spectra, which may trace the progenitor's internal composition. USSNe are also predicted to synthesize little to no ^{56}Ni, consistent with our bolometric light-curve modelling. In the EC SN channel, the ejecta mass is expected to be very low, which is compatible with the overall fast evolution of SN 2024abvb. However, the predicted ejecta masses for EC SNe ($\leq 0.2, M_{\odot}$; Tauris et al. 2015) are significantly smaller than the value inferred from our modelling.

Moriya et al. (2025) presented light-curve models for USSNe interacting with CSM, predicting a rapid rise to peak (~ 8 days) followed by a relatively slow decline over ~ 20 days. These behaviours closely resemble the bolometric light curve of SN 2024abvb (Figure 11). Their models further suggest ejecta energies of 10^{50} erg, which align well with our best-fitting parameters and CSM masses of ~ 0.2 $M_{\odot}$, again comparable to our results. The primary caveat for adopting this interpretation is the ejecta mass, which in their models (~0.06 $M_{\odot}$) is substantially smaller than the value we infer (3.9 $M_{\odot}$) and only one order of magnitude smaller than the MCMC best fit, albeit retrieved with a high χ^2 although we infer a much closer value from our MCMC driven light curves of M_{ej} = 0.43 M$_{\odot}$ while this is still larger, it is significantly closer in agreement than our previous estimate. We note that Hu et al. (2026) report M_{ej} = 0.12 M$_{\odot}$ from their MOSFiT fit. This discrepancy could arise from differences in the theoretical prescriptions implemented in MOSFiT, from different opacity assumptions, or from differences in the datasets as we have additional broadband imaging points during the rise and beyond 15 days after maximum light. Their MOSFiT posterior distribution shows a lower χ^2 than ours, implying a better fit to the dataset. However, such codes assume spherical symmetry for both the ejecta and the CSM, whereas for SN 2024abvb INTEL Collaboration (2026) reported CSM asymmetries of up to 4%. This indicates an additional source of uncertainty in outputs from simple semi-analytical models.

The remaining unresolved aspect across all progenitor scenarios considered is the unusually low observed temperature. This, however, can be explained through alternative processes, such as the formation of a cool/cold dense shell (CDS) (Chugai et al. 2004) with temperatures of $\sim 10^4$K at the interface between the ejecta and the CSM. A denser CSM could lead to an optically thick environment in which radiation remains trapped, undergoing adiabatic losses that reduce the effective temperature despite strong instantaneous shock heating (Chugai et al. 2004; Nymark et al. 2006). Aspherical CSM distributions can produce lower effective temperatures due to an increased radiating area (Dessart et al. 2015; Suzuki et al. 2019). Moreover, simulations of supernova explosions interacting with aspherical CSM distributions show that shock heating, density enhancement, and radiative diffusion depend strongly on the CSM geometry (Kurfürst et al. 2020). INTEL Collaboration (2026) proposed that concentric toroidal shells could account for the relatively high asphericity ($P \sim 4\%$) of SN 2024abvb, as well as for the structure observed in their higher-resolution spectra. Clumpy CSM structures can create similar outcomes, as the shock propagates through regions of varying density, generating temperature behaviour consistent with CDS-like cooling (Chugai & Danziger 1994; Chandra 2018). A decrease in the optical depth of the CSM (INTEL Collaboration 2026), driven by expansion, can expose cooler and deeper layers or modify the effective photosphere, leading to a lower inferred temperature (Nicholl 2021). Such effects are more likely in binary scenarios, where asphericity is expected to be more pronounced, and can therefore result in systematically lower observed temperatures compared to symmetric configurations.

6 SUMMARY AND CONCLUSIONS

We have presented spectroscopic and photometric observations of SN 2024abvb, a Type Ibn/Icn event that exhibits several properties distinct from the broader Type Ibn/Icn SN population, including an unusually large projected separation from its presumed host galaxy (21.5 kpc). The combined spectroscopic and photometric dataset highlights how atypical SN 2024abvb is relative to other hydrogen- and helium-deficient interacting supernovae.

SN 2024abvb displays a g-band rise time notably longer than that of typical Type Icn, and Ibn, events. The ATLAS o-band rise time is also marginally extended relative to other Type Icns. All photometric bands exhibit linear post-peak declines, with the steepest fading observed in the UV and blue optical filters, and the shallowest in the NIR. This behaviour is consistent with sustained high-energy photon reprocessing.

In the r-band, SN 2024abvb declines at a rate comparable to other Type Icn events but peaks at a higher luminosity. This suggests a similar low-mass CSM environment and progenitor pathway as for SN 2019hgp, albeit with a slightly higher peak magnitude ($M_r \approx -19.2$ mag), indicative of a more efficient conversion of shock energy into radiation.

The bolometric light curve of SN 2024abvb declines approximately linearly after peak, but the peak black-body temperature is substantially lower than that found in other interacting Type Ibn/Icn SNe. The fractional flux evolution confirms that UV emission dominates at early times, with optical flux rising to match the UV contribution as the ejecta–CSM interaction proceeds. The NIR fraction initially decreases and then stabilises slightly above its early value, suggesting minimal dust formation or dust formation occurring after the epochs probed by our last NIR observations. The overall bolometric evolution resembles the CSM-interaction USSN models of Moriya et al. (2025), with the exception of the larger ejecta mass inferred for SN 2024abvb.

Spectroscopically, SN 2024abvb exhibits an initially blue continuum with multiple narrow P-Cygni features, dominated by C II λ5890 in emission. The continuum temperature decreases with time, reaching a plateau after ~20 days, likely due to metal-line blanketing. Weak He I λ5876 absorption is detected in the earliest medium-resolution spectra, and the same spectra reveal a broad red-wing shoulder associated with C II λ5890, further suggesting heavy metal-line blanketing or possibly an asymmetric CSM configuration.

O II λ4651 is present in the early-time spectra, broadens at intermediate epochs, and disappears at later times. In contrast, C II λ5890 persists throughout the observed period, transitioning to a P-Cygni profile in both low- and medium-resolution spectra after ~20 days. The medium-resolution data also show H I λ4861, O II λ4651, and Fe II λ5363 with discernible P-Cygni features even at late times.

Comparisons with other Type Icn and Type Ibn SNe reinforce the uniqueness of SN 2024abvb. While some similarities exist, the spectra and photometric evolution strongly disfavour a Type Ibn classification and instead support a carbon-rich, low-mass CSM environment consistent with an Type Ibn/Icn SN.

The expansion velocities of SN 2024abvb peak at values compatible with canonical WR wind speeds. However, the subsequent decline is inconsistent with expectations for an unshocked WR-like wind or shell. This suggests that the CSM may have been produced either by a discrete eruptive episode or by binary interaction. In an eruptive scenario, the implied mass-loss rate would be high enough to dominate the local density structure, while a steady WR wind alone would struggle to reproduce the observed CSM properties. The velocities are comparable to those of other interacting SNe but point toward a progenitor pathway more complex than that of a single WR star.

It is unlikely that SN 2024abvb originated from a thermonuclear (Type Ia) explosion; the corresponding light curves are incompatible with those observed. A scenario involving a rare massive star formed in a low-star-formation region also appears improbable given the extremely low local SFR. The most plausible explanation is that SN 2024abvb was an USSNe, a scenario capable of accounting for most of its observed properties and naturally explaining the extreme separation from the host. However, this interpretation does not reconcile the discrepancy between the ejecta mass inferred for SN 2024abvb and the significantly lower ejecta masses predicted by current USSNe models (e.g. Tauris et al. 2017; Moriya et al. 2025).

Ultimately, advancing our understanding of interacting SNe will require a larger sample of well-observed events, with dense photometric coverage and, crucially, higher-resolution spectroscopy and spectropolarimetry to probe potential asymmetries in their ejecta and circumstellar environments. Such datasets are essential for disentangling the diverse progenitor channels that give rise to interacting explosions and for clarifying the roles of single and binary evolution in shaping their observable properties. With improved observational constraints, we can move toward a more complete and physically grounded picture of the late-stage evolution of massive stars and the mechanisms that produce these rare and intriguing transients.

ACKNOWLEDGEMENTS

CI gratefully acknowledges the support received from the MERAC Foundation. T.E.M.B. is funded by Horizon Europe ERC grant no.

101125877. J.R.F. is supported by the U.S. National Science Foundation (NSF) Graduate Research Fellowship Program under grant 2139319. CPG acknowledges financial support from the Secretary of Universities and Research (Government of Catalonia) and by the Horizon 2020 Research and Innovation Programme of the European Union under the Marie Skłodowska-Curie and the Beatriu de Pinós 2021 BP 00168 programme, from the Spanish Ministerio de Ciencia e Innovación (MCIN) and the Agencia Estatal de Investigación (AEI) 10.13039/501100011033 under the PID2023-151307NB-I00 SNNEXT project, from Centro Superior de Investigaciones Científicas (CSIC) under the PIE project 20215AT016 and the program Unidad de Excelencia María de Maeztu CEX2020-001058-M, and from the Departament de Recerca i Universitats de la Generalitat de Catalunya through the 2021-SGR-01270 grant. TLK acknowledges support via a Warwick Astrophysics prize post-doctoral fellowship made possible thanks to a generous philanthropic donation. GL was supported by a research grant (VIL60862) from VILLUM FONDEN. SM is funded by Leverhulme Trust grant RPG-2023-240. MP acknowledges support from a UK Research and Innovation Fellowship (MR/T020784/1 and UKRI1062). Based on observations collected at Copernico and Schmidt telescopes (Asiago Mount Ekar, Italy) of the INAF – Osservatorio Astronomico di Padova. AR acknowledges financial support from the GRAWITA Large Program Grant (PI P. D'Avanzo). AR, AP, GV acknowledge financial support from the PRIN-INAF 2022 "Shedding light on the nature of gap transients: from the observations to the models" BW acknowledges the UKRI's STFC studentship grant funding, project reference ST/X508871/1 FEB acknowledges support from ANID-Chile BASAL CATA FB210003, FONDECYT Regular 1241005, and Millennium Science Initiative, AIM23-0001. T.-W.C. acknowledges support from the Ministry of Education Yushan Fellow Program (MOE-111-YSFMS-0008-001-P1) and from the National Science and Technology Council, Taiwan (NSTC 114-2112-M-008-021-MY3). G.V. and A.R. acknowledge financial support from the SOXS project (PI S. Campana). This article is also based on observations obtained from the La Silla Observatory with the REM telescope, under the program REM AOT47-37 (ID 49337, PI: G. Valerin). KAB is supported by an LSST-DA Catalyst Fellowship; this publication was thus made possible through the support of Grant 62192 from the John Templeton Foundation to LSST-DA. JDL acknowledges support from a UK Research and Innovation Future Leaders Fellowship (grant references MR/T020784/1 and UKRI1062).

Based on observations collected at the European Organisation for Astronomical Research in the Southern Hemisphere, Chile, as part of ePESSTO+ (the advanced Public ESO Spectroscopic Survey for Transient Objects Survey – PI: Inserra). ePESSTO+ observations were obtained under ESO program ID 112.25JQ. This work makes use of data from the Asteroid Terrestrial-impact Last Alert System (ATLAS) project. The ATLAS project is primarily funded by NASA grants. The Gravitational-wave Optical Transient Observer (GOTO) project acknowledges the support of the Monash-Warwick Alliance; University of Warwick; Monash University; University of Sheffield; University of Leicester; Armagh Observatory & Planetarium; the National Astronomical Research Institute of Thailand (NARIT); Instituto de Astrofísica de Canarias (IAC); University of Portsmouth; University of Turku; University of Manchester and the UK Science and Technology Facilities Council (STFC, grant numbers ST/T007184/1, ST/T003103/1 and ST/T000406/1). This article includes observations made in the Two-meter Twin Telescope (TTT) in the Teide Observatory of the IAC, that Light Bridges operates in the Island of Tenerife, Canary Islands (Spain). The Observing Time Rights (DTO) used for this research were provided by Light Bridges, SL. This paper uses data that were obtained by The Legacy Surveys: the Dark Energy Camera Legacy Survey (DECaLS; NOAO Proposal ID # 2014B-0404; PIs: David Schlegel and Arjun Dey), the Beijing-Arizona Sky Survey (BASS; NOAO Proposal ID # 2015A-0801; PIs: Zhou Xu and Xiaohui Fan), and the Mayall z-band Legacy Survey (MzLS; NOAO Proposal ID # 2016A-0453; PI: Arjun Dey). DECaLS, BASS and MzLS together include data obtained, respectively, at the Blanco telescope, Cerro Tololo Inter-American Observatory, National Optical Astronomy Observatory (NOAO); the Bok telescope, Steward Observatory, University of Arizona; and the Mayall telescope, Kitt Peak National Observatory, NOAO. NOAO is operated by the Association of Universities for Research in Astronomy (AURA) under a cooperative agreement with the National Science Foundation. Please see http://legacysurvey.org for details regarding the Legacy Surveys. BASS is a key project of the Telescope Access Program (TAP), which has been funded by the National Astronomical Observatories of China, the Chinese Academy of Sciences (the Strategic Priority Research Program "The Emergence of Cosmological Structures" Grant No. XDB09000000), and the Special Fund for Astronomy from the Ministry of Finance. The BASS is also supported by the External Cooperation Program of Chinese Academy of Sciences (Grant No. 114A11KYSB20160057) and Chinese National Natural Science Foundation (Grant No. 11433005). The Legacy Surveys imaging of the DESI footprint is supported by the Director, Office of Science, Office of High Energy Physics of the U.S. Department of Energy under Contract No. DE-AC02-05CH1123, and by the National Energy Research Scientific Computing Center, a DOE Office of Science User Facility under the same contract; and by the U.S. National Science Foundation, Division of Astronomical Sciences under Contract No.AST-0950945 to the National Optical Astronomy Observatory. The VISTA Hemisphere Survey data products served at Astro Data Lab are based on observations collected at the European Organisation for Astronomical Research in the Southern Hemisphere under ESO programme 179.A-2010, and/or data products created thereof. Pan-STARRS is a project of the Institute for Astronomy of the University of Hawaii, and is supported by the NASA SSO Near Earth Observation Program under grants 80NSSC18K0971, NNX14AM74G, NNX12AR65G, NNX13AQ47G, NNX08AR22G, 80NSSC21K1572 and by the State of Hawaii. This work makes use of observations from the Las Cumbres Observatory network. The LCO team is supported by NSF grants AST-2308113 and AST-1911151.

DATA AVAILABILITY

Photometry data are listed in the appendix. All spectra are available on WISeREP (https://www.wiserep.org).

REFERENCES

Ambikasaran S., Foreman-Mackey D., Greengard L., Hogg D. W., O'Neil M., 2015, IEEE Transactions on Pattern Analysis and Machine Intelligence, 38, 252

Bellm E. C., et al., 2019, PASP, 131, 018002

Brown T. M., et al., 2013, PASP, 125, 1031

Buzzoni B., et al., 1984, The Messenger, 38, 9

Cardelli J. A., Clayton G. C., Mathis J. S., 1989, ApJ, 345, 245

Chabrier G., 2003, PASP, 115, 763

Chambers K. C., et al., 2019, The Pan-STARRS1 Surveys (`arXiv:1612.05560`), `https://arxiv.org/abs/1612.05560`

Chandra P., 2018, Space Science Reviews, 214

Chatzopoulos E., Wheeler J. C., 2012, ApJ, 748, 42

Chevalier R. A., Fransson C., 1994, ApJ, 420, 268

Chevalier R. A., Fransson C., 2017, in Alsabti A. W., Murdin P., eds, , Handbook of Supernovae. Springer International Publishing, p. 875, doi:10.1007/978-3-319-21846-5_34

Chiba R., Moriya T. J., 2024, ApJ, 973, 14

Chugai N. N., Danziger I. J., 1994, MNRAS, 268, 173

Chugai N. N., et al., 2004, MNRAS, 352, 1213

Conroy C., Gunn J. E., White M., 2009, ApJ, 699, 486

Covino S., et al., 2002, in Favata F., Drake J. J., eds, Astronomical Society of the Pacific Conference Series Vol. 277, Stellar Coronae in the Chandra and XMM-NEWTON Era. p. 449 (`arXiv:astro-ph/0109411`), doi:10.48550/arXiv.astro-ph/0109411

Crowther P. A., 2007a, ARA&A, 45, 177

Crowther P. A., 2007b, Annual Review of Astronomy and Astrophysics, 45, 177

Dalton G. B., et al., 2006, in McLean I. S., Iye M., eds, Society of Photo-Optical Instrumentation Engineers (SPIE) Conference Series Vol. 6269, Ground-based and Airborne Instrumentation for Astronomy. p. 62690X, doi:10.1117/12.670018

Davis K. W., et al., 2023, Monthly Notices of the Royal Astronomical Society, 523, 2530–2550

Dessart L., Audit E., Hillier D. J., 2015, MNRAS, 449, 4304

Dessart L., Hillier D. J., Kuncarayakti H., 2022, A&A, 658, A130

Dey A., et al., 2019, The Astronomical Journal, 157, 168

Djupvik A. A., Andersen J., 2010, in Diego J. M., Goicoechea L. J., González-Serrano J. I., Gorgas J., eds, Astrophysics and Space Science Proceedings Vol. 14, Highlights of Spanish Astrophysics V. p. 211 (`arXiv:0901.4015`), doi:10.1007/978-3-642-11250-8_21

Doliva-Dolinsky A., et al., 2025, The NGC3109 Satellite System: The First Systematic Resolved Search for Dwarf Galaxies Around a SMC-mass Host (`arXiv:2505.05570`), `https://arxiv.org/abs/2505.05570`

Drout M. R., et al., 2014, ApJ, 794, 23

Dyer M. J., et al., 2024, The Gravitational-wave Optical Transient Observer (GOTO) (`arXiv:2407.17176`), `https://arxiv.org/abs/2407.17176`

Eldridge J. J., Langer N., Tout C. A., 2011, MNRAS, 414, 3501

Eldridge J. J., Fraser M., Smartt S. J., Maund J. R., Crockett R. M., 2013, MNRAS, 436, 774

Emerson J., McPherson A., Sutherland W., 2006, The Messenger, 126, 41

Filippenko A. V., 1997, ARA&A, 35, 309

Foley R. J., Smith N., Ganeshalingam M., Li W., Chornock R., Filippenko A. V., 2007, ApJ, 657, L105

Foley R. J., et al., 2013, The Astrophysical Journal, 767, 57

Foreman-Mackey D., Hogg D. W., Lang D., Goodman J., 2013, Publications of the Astronomical Society of the Pacific, 125, 306–312

Gal-Yam A., et al., 2022, Nature, 601, 201

Gallazzi A., Charlot S., Brinchmann J., White S. D. M., Tremonti C. A., 2005, MNRAS, 362, 41

Geha M., Blanton M. R., Yan R., Tinker J. L., 2012, The Astrophysical Journal, 757, 85

Groot P. J., et al., 2024, PASP, 136, 115003

Hainich R., et al., 2014, A&A, 565, A27

Hamann W.-R., et al., 2019, A&A, 625, A57

Hosseinzadeh G., et al., 2017, ApJ, 836, 158

Hosseinzadeh G., McCully C., Zabludoff A. I., Arcavi I., French K. D., Howell D. A., Berger E., Hiramatsu D., 2019, The Astrophysical Journal Letters, 871, L9

Hu M., et al., 2026, SN 2024abvb: A Type Icn Supernova in the Outskirts of its Host Galaxy (`arXiv:2601.01333`), `https://arxiv.org/abs/2601.01333`

Hunter D. J., et al., 2009, A&A, 508, 371

INTEL Collaboration 2026, arXiv e-prints, p. arXiv:2602.00389

Inserra C., et al., 2018, MNRAS, 475, 1046

Irrgang A., Kreuzer S., Heber U., 2018, A&A, 620, A48

Jedicke R., Tonry J., Veres P., Farnocchia D., Spoto F., Rest A., Wainscoat R. J., Lee E., 2012, in AAS/Division for Planetary Sciences Meeting Abstracts #44. p. 210.12

Jha S., Branch D., Chornock R., Foley R. J., Li W., Swift B. J., Casebeer D., Filippenko A. V., 2006, AJ, 132, 189

Johnson B. D., Leja J., Conroy C., Speagle J. S., 2021, ApJS, 254, 22

Jordan G. C., Perets H. B., Fisher R. T., van Rossum D. R., 2012, The Astrophysical Journal, 761, L23

Kasen D., Woosley S. E., 2009, The Astrophysical Journal, 703, 2205

Komatsu E., et al., 2011, ApJS, 192, 18

Kudritzki R.-P., Puls J., 2000, ARA&A, 38, 613

Kurfürst P., Pejcha O., Krtička J., 2020, A&A, 642, A214

Lyman J. D., Bersier D., James P. A., Mazzali P. A., Eldridge J. J., Fraser M., Pian E., 2016, MNRAS, 457, 328

Magnier E., 2006, in Ryan S., ed., The Advanced Maui Optical and Space Surveillance Technologies Conference. p. E50

Magnier E. A., et al., 2020, The Astrophysical Journal Supplement Series, 251, 6

Mattila S., et al., 2008, MNRAS, 389, 141

McCully C., et al., 2014, Nature, 512, 54

Meynet G., Maeder A., 2005, A&A, 429, 581

Minkowski R., 1941, PASP, 53, 224

Moriya T. J., Mueller B., Blinnikov S. I., Ushakova M., Sorokina E. I., Tauris T. M., Heger A., 2025, Type Ibn supernovae from ultra-stripped supernova progenitors (`arXiv:2507.05506`), `https://arxiv.org/abs/2507.05506`

Nagao T., et al., 2023, A&A, 673, A27

Newville M., Stensitzki T., Allen D. B., Ingargiola A., 2014, LMFIT: Non-Linear Least-Square Minimization and Curve-Fitting for Python, doi:10.5281/zenodo.11813, `https://doi.org/10.5281/zenodo.11813`

Nicholl M., 2021, Astronomy and Geophysics, 62, 5.34

Nomoto K., 1987, Astrophysical Journal, Part 1 (ISSN 0004-637X), vol. 322, Nov. 1, 1987, p. 206-214., 322, 206

Nymark T. K., Fransson C., Kozma C., 2006, A&A, 449, 171

Pastorello A., et al., 2007, Nature, 447, 829

Pastorello A., et al., 2015, MNRAS, 449, 1921

Pellegrino C., et al., 2022, The Astrophysical Journal, 938, 73

Perets H. B., 2008, The Astrophysical Journal, 690, 795–801

Perets H. B., et al., 2010, Nature, 465, 322

Perley D. A., et al., 2022, The Astrophysical Journal, 927, 180

Pignata G., et al., 2004, MNRAS, 355, 178

Prentice S. J., et al., 2018, MNRAS, 478, 4162

Pursiainen M., et al., 2023, ApJ, 959, L10

Sander A. A. C., Hamann W.-R., Todt H., Hainich R., Shenar T., Ramachandran V., Oskinova L. M., 2019, A&A, 621, A92

Schlafly E. F., Finkbeiner D. P., 2011, ApJ, 737, 103

Schulze S., et al., 2025, Nature, 644, 634

Sharina M. E., 2019, Astrophysics, 62, 9–17

Shi J., et al., 2026, arXiv e-prints, p. arXiv:2602.16227

Smartt S. J., et al., 2015, A&A, 579, A40

Smith N., 2017, Interacting Supernovae: Types IIn and Ibn. Springer International Publishing, p. 403–429, doi:10.1007/978-3-319-21846-5_38, `http://dx.doi.org/10.1007/978-3-319-21846-5_38`

Smith L. F., Aller L. H., 1971, ApJ, 164, 275

Smith N., McCray R., 2007, ApJ, 671, L17

Smith N., Li W., Filippenko A. V., Chornock R., 2011, Monthly Notices of the Royal Astronomical Society, 412, 1522–1538

Srivastav S., et al., 2022, MNRAS, 511, 2708

Steeghs D., et al., 2022a, MNRAS, 511, 2405

Steeghs D., et al., 2022b, Monthly Notices of the Royal Astronomical Society, 511, 2405–2422

Stritzinger M., et al., 2002, AJ, 124, 2100

Stritzinger M., Fraser M., Pastorello A., Hoogendam W., Morrell N., Gutiérrez C., 2024, Transient Name Server Classification Report, 2024-4674, 1

Sukhbold T., Ertl T., Woosley S. E., Brown J. M., Janka H.-T., 2016, The Astrophysical Journal, 821, 38

Suzuki A., Moriya T. J., Takiwaki T., 2019, The Astrophysical Journal, 887, 249

Tauris T. M., Langer N., Moriya T. J., Podsiadlowski P., Yoon S.-C., Blinnikov S. I., 2013, The Astrophysical Journal Letters, 778, L23

Tauris T. M., Langer N., Podsiadlowski P., 2015, Ultra-stripped supernovae: progenitors and fate (arXiv:1505.00270), https://arxiv.org/abs/1505.00270
Tauris T. M., et al., 2017, The Astrophysical Journal, 846, 170
Tonry J. L., et al., 2018, PASP, 130, 064505
Tonry J., et al., 2024, Transient Name Server Discovery Report, 2024-4579, 1
Torres A. V., Conti P. S., 1984, ApJ, 280, 181
Vázquez-Semadeni E., Gómez G. C., Jappsen A.-K., Ballesteros-Paredes J., Klessen R. S., 2009, ApJ, 707, 1023
Watkins L. L., van der Marel R. P., Sohn S. T., Wyn Evans N., 2019, The Astrophysical Journal, 873, 118
Wheeler J. C., Levreault R., 1985, ApJ, 294, L17
Woosley S. E., Langer N., Weaver T. A., 1995, ApJ, 448, 315
Wu C., et al., 2024, The Astrophysical Journal Letters, 967, L45
Yaron O., Gal-Yam A., 2012, PASP, 124, 668

APPENDIX A: DATA TABLES

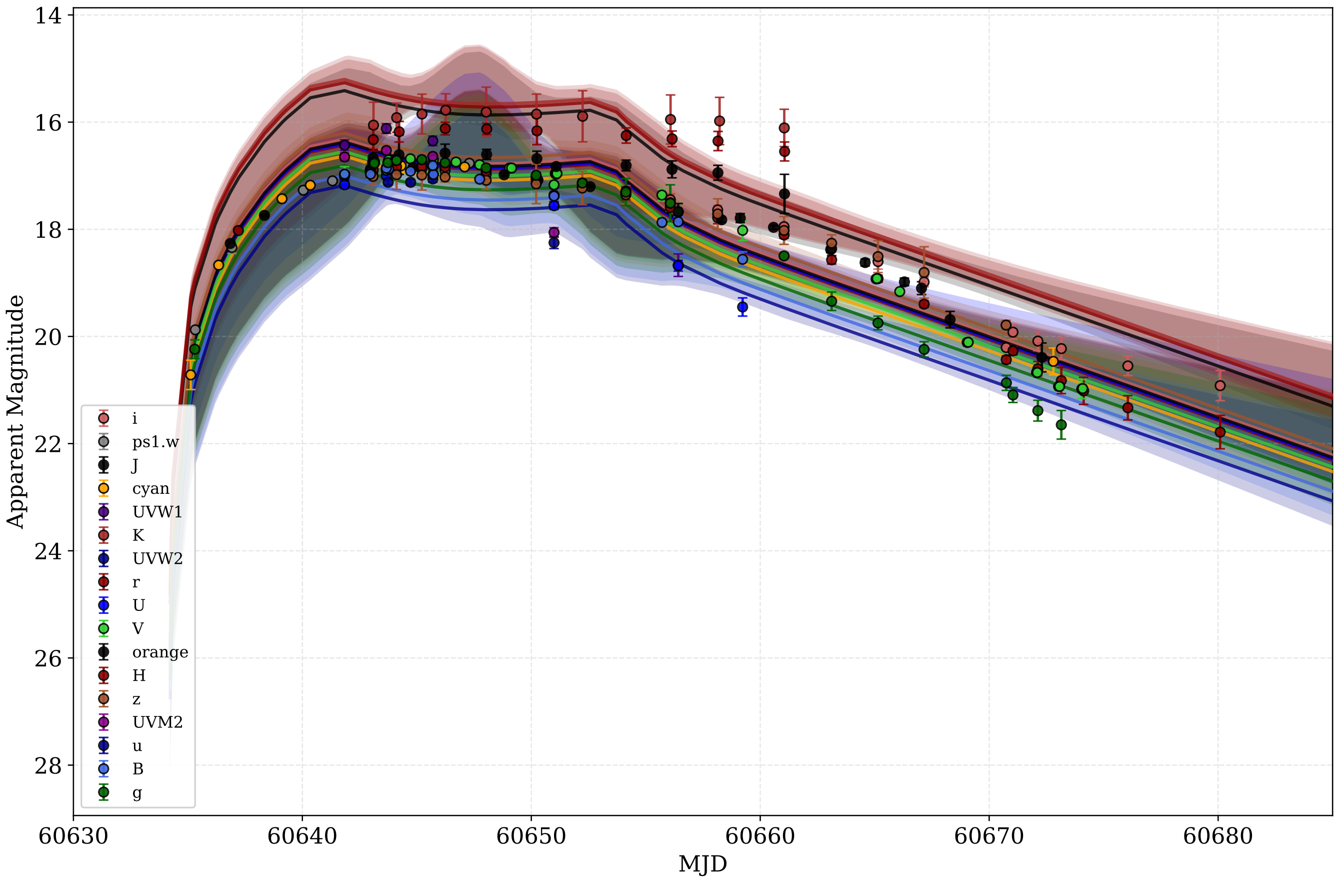

Figure A1.

Table A1. Table of all spectral observations. This table is also available as supplementary material.

Date of obs	MJD	Rest frame phase (w.r.t maximum in days)	Instrument	Grism	Slit	Resolution (Å)
2024-11-27	60641.90	-3.2	NOT/ALFOSC	Gr4	1.0"	16.2
2024-11-29	60643.08	-2.1	NTT/EFOSC2	Gr11,Gr16,Gr18	1.0"	17.16, 17.29, 8.19
2024-11-30	60644.06	-1.1	NTT/EFOSC2	Gr11,Gr16,Gr18	1.0"	17.16, 17.29, 8.19
2024-12-02	60646.22	1.1	FLOYDS		2.0"	17.0
2024-12-05	60649.05	3.9	NTT/EFOSC2	Gr11,Gr16,Gr18	1.0"	17.16, 17.29, 8.19
2024-12-07	60651.05	5.9	NTT/EFOSC2	Gr11,Gr16,Gr18	1.0"	17.16, 17.29, 8.19
2024-12-08	60652.21	7.1	FLOYDS		2.0"	17.0
2024-12-19	60663.27	18.1	FLOYDS		2.0"	17.0
2024-12-21	60665.06	19.9	NTT/EFOSC2	Gr11,Gr16	1.0"	17.16, 17.29
2024-12-22	60666.10	21.0	NTT/EFOSC2	Gr18	1.0"	8.19
2024-12-25	60669.04	23.9	NTT/EFOSC2	Gr11,Gr16	1.0"	17.16, 17.29
2024-12-29	60673.03	27.9	NTT/EFOSC2	Gr16	1.0"	17.29
2024-12-30	60674.04	28.9	NTT/EFOSC2	Gr18	1.0"	8.19

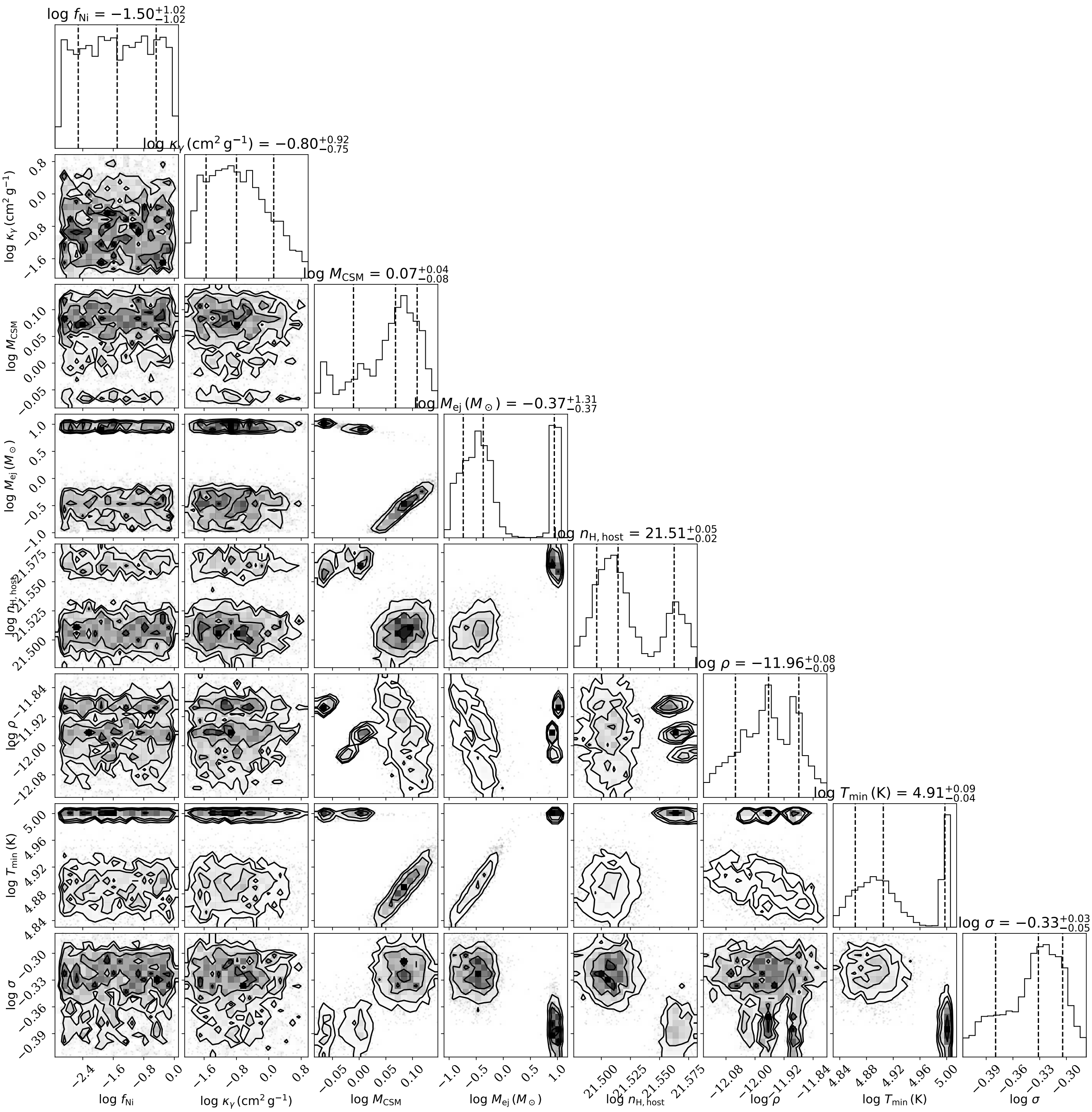
log $f_{\rm Ni}$ = $-1.50^{+1.02}_{-1.02}$
log κ_γ (cm^2 g^{-1}) = $-0.80^{+0.92}_{-0.75}$
log $M_{\rm CSM}$ = $0.07^{+0.04}_{-0.08}$
log $M_{\rm ej}$ ($M_\odot$) = $-0.37^{+1.31}_{-0.37}$
log $n_{\rm H,host}$ = $21.51^{+0.05}_{-0.02}$
log ρ = $-11.96^{+0.08}_{-0.09}$
log $T_{\rm min}$ (K) = $4.91^{+0.09}_{-0.04}$
log σ = $-0.33^{+0.03}_{-0.05}$
log $f_{\rm Ni}$
log κ_γ (cm^2 g^{-1})
log $M_{\rm CSM}$
log $M_{\rm ej}$ ($M_\odot$)
log $n_{\rm H,host}$
log ρ
log $T_{\rm min}$ (K)
log σ

Figure A2.

Table A2: A table displaying all photometric data used. This table is also available as supplementary material.

MJD	Band	mag	err	marker
60641.84	B	16.970	0.080	UVOT
60642.97	B	16.971	0.100	NOT
60643.67	B	16.860	0.060	UVOT
60643.77	B	16.876	0.027	67/91,Moravian
60644.72	B	16.916	0.025	67/91,Moravian
60644.84	B	16.835	0.013	LCO
60644.84	B	16.827	0.014	LCO
60645.70	B	16.810	0.060	UVOT
60645.73	B	16.977	0.032	67/91,Moravian
60646.72	B	16.022	0.036	67/91,Moravian
60646.83	B	16.937	0.015	LCO
60646.83	B	16.949	0.014	LCO
60647.75	B	17.065	0.058	67/91,Moravian
60648.10	B	17.054	0.024	LCO
60648.11	B	17.043	0.024	LCO
60650.04	B	17.258	0.017	LCO
60650.04	B	17.266	0.018	LCO
60650.99	B	17.380	0.080	UVOT
60651.85	B	17.348	0.017	LCO
60651.85	B	17.351	0.017	LCO
60655.71	B	17.871	0.068	67/91,Moravian
60655.94	B	17.811	0.032	LCO
60655.94	B	17.855	0.029	LCO
60656.42	B	17.860	0.090	UVOT
60658.82	B	18.426	0.035	LCO
60658.83	B	18.442	0.036	LCO
60659.23	B	18.560	0.140	UVOT
60664.10	B	19.770	0.029	LCO
60664.11	B	19.771	0.031	LCO
60667.11	B	20.662	0.120	LCO
60667.11	B	20.466	0.092	LCO
60669.71	B	>20.120	-	67/91,Moravian
60675.04	B	21.518	0.154	LCO
60675.04	B	22.408	0.282	LCO
60678.05	B	22.076	0.248	LCO
60690.05	B	20.967	0.222	LCO
60693.04	B	22.054	0.429	LCO
60693.04	B	22.311	0.416	LCO
60683.81	B	>21.711	-	Liverpool
60641.84	V	16.98	0.15	UVOT
60642.97	V	16.906	0.1	NOT
60643.08	V	16.75	0.054	NTT
60643.08	V	16.746	0.023	NTT
60643.15	V	16.741	0.042	NTT
60643.67	V	16.9	0.12	UVOT
60643.77	V	16.705	0.027	67/91,Moravian
60644.05	V	16.712	0.042	NTT
60644.06	V	16.714	0.036	NTT
60644.14	V	16.705	0.04	NTT
60644.72	V	16.685	0.024	67/91,Moravian
60644.84	V	16.718	0.016	LCO
60644.85	V	16.723	0.018	LCO
60645.7	V	16.84	0.1	UVOT
60645.72	V	16.704	0.023	67/91,Moravian
60646.71	V	16.745	0.035	67/91,Moravian
60646.83	V	16.794	0.018	LCO
60646.83	V	16.797	0.018	LCO

Table A2 continued from previous page

MJD	Band	mag	err	marker
60647.74	V	16.796	0.037	67/91,Moravian
60648.11	V	16.88	0.065	LCO
60648.11	V	16.879	0.046	LCO
60649.05	V	16.856	0.024	NTT
60649.14	V	16.857	0.044	NTT
60650.04	V	17.008	0.015	LCO
60650.05	V	16.982	0.015	LCO
60650.99	V	17.17	0.13	UVOT
60651.05	V	16.957	0.02	NTT
60651.08	V	16.971	0.026	NTT
60651.12	V	16.96	0.038	NTT
60651.85	V	17.093	0.019	LCO
60651.85	V	17.108	0.021	LCO
60655.7	V	17.361	0.109	67/91,Moravian
60655.95	V	17.121	0.206	LCO
60655.95	V	16.787	0.201	LCO
60656.42	V	17.67	0.15	UVOT
60658.83	V	17.837	0.027	LCO
60658.83	V	17.925	0.029	LCO
60659.23	V	18.02	0.19	UVOT
60664.11	V	18.821	0.028	LCO
60664.11	V	18.789	0.028	LCO
60665.06	V	18.926	0.034	NTT
60665.11	V	18.919	0.025	NTT
60666.09	V	19.162	0.04	NTT
60667.12	V	19.508	0.064	LCO
60667.12	V	19.77	0.07	LCO
60669.04	V	20.111	0.064	NTT
60669.09	V	20.108	0.078	NTT
60669.7	V	>19.947	-	67/91,Moravian
60672.07	V	20.672	0.071	NTT
60672.11	V	20.673	0.066	NTT
60673.03	V	20.932	0.082	NTT
60673.08	V	20.933	0.076	NTT
60674.04	V	20.981	0.18	NTT
60674.09	V	20.972	0.094	NTT
60675.05	V	21.159	0.152	LCO
60675.05	V	21.422	0.185	LCO
60678.06	V	21.496	0.321	LCO
60678.06	V	21.391	0.281	LCO
60683.82	V	>20.399	-	Liverpool
60687.06	V	21.037	0.321	LCO
60690.06	V	21.049	0.38	LCO
60641.84	U	17.17	0.07	UVOT
60643.67	U	17	0.06	UVOT
60643.75	U	17.121	0.05	67/91,Moravian
60644.73	U	17.124	0.05	67/91,Moravian
60645.7	U	16.98	0.05	UVOT
60650.99	U	17.56	0.07	UVOT
60656.42	U	18.68	0.1	UVOT
60659.23	U	19.45	0.17	UVOT
60614.36	g	>21.124	-	ZTF
60622.19	g	>20.420	-	ZTF
60632.13	g	>20.180	-	ZTF
60634.25	g	>20.764	-	ZTF
60635.3	g	20.238	0.174	ZTF
60637.23	g	>20.239	-	ZTF
60639.31	g	>16.841	-	ZTF
60642.82	g	16.910	0.016	TTT
60642.98	g	16.699	0.013	LCO

Table A2 continued from previous page

MJD	Band	mag	err	marker
60642.99	g	16.892	0.016	TTT
60643.09	g	16.781	0.182	REM
60643.15	g	16.767	0.041	ZTF
60643.73	g	16.757	0.022	67/91,Moravian-DIF
60643.97	g	16.830	0.022	TTT
60644.11	g	16.718	0.027	REM
60644.81	g	16.665	0.011	LCO
60644.82	g	16.870	0.016	TTT
60645.01	g	16.855	0.019	TTT
60645.22	g	16.7	0.041	REM
60646.23	g	16.76	0.056	REM
60646.79	g	16.787	0.012	LCO
60646.82	g	16.946	0.026	TTT
60647.82	g	17.036	0.016	TTT
60647.99	g	17.024	0.018	TTT
60648.03	g	16.855	0.057	REM
60649.08	g	16.94	0.013	LCO
60650.21	g	16.992	0.05	REM
60650.85	g	17.124	0.014	LCO
60652.23	g	17.137	0.065	REM
60654.13	g	17.306	0.253	REM
60656.07	g	17.514	0.344	REM
60656.46	g	17.683	0.032	LCO
60658.46	g	18.108	0.039	LCO
60660.46	g	18.526	0.058	LCO
60661.04	g	18.497	0.05	REM
60662.92	g	18.991	0.063	LCO
60663.12	g	19.343	0.172	REM
60664.46	g	19.42	0.056	LCO
60665.14	g	19.748	0.127	REM
60666.81	g	20.193	0.115	LCO
60667.16	g	20.242	0.144	REM
60668.47	g	20.51	0.15	LCO
60670.75	g	20.866	0.141	AFOSC
60671.03	g	21.092	0.14	REM
60672.13	g	21.385	0.194	REM
60672.46	g	21.597	0.324	LCO
60673.15	g	21.649	0.267	REM
60675.06	g	21.308	0.272	LCO
60676.06	g	>21.623	-	REM
60680.09	g	>21.646	-	REM
60683.82	g	>20.642	-	Liverpool
57406.24	r	>22.773	-	PS1
60614.2	r	>20.779	-	ZTF
60616.33	r	>21.216	-	ZTF
60616.33	r	21.72	0.462	ZTF
60619.17	r	>20.953	-	ZTF
60620.14	r	>20.294	-	ZTF
60622.17	r	>20.880	-	ZTF
60625.33	r	>19.996	-	ZTF
60632.23	r	>20.951	-	ZTF
60634.23	r	>20.410	-	ZTF
60635.17	r	>20.817	-	ZTF
60637.2	r	18.023	0.021	ZTF
60642.97	r	16.91	0.121	NOT
60642.98	r	16.851	0.017	LCO
60643.09	r	16.885	0.029	REM
60643.74	r	16.867	0.024	67/91,Moravian-DIF
60644.11	r	16.836	0.063	REM
60644.81	r	16.822	0.012	LCO

Table A2 continued from previous page

MJD	Band	mag	err	marker
60645.22	r	16.824	0.067	REM
60646.23	r	16.837	0.034	REM
60646.79	r	16.846	0.011	LCO
60648.03	r	16.914	0.022	REM
60649.08	r	17.024	0.015	LCO
60650.21	r	17.03	0.029	REM
60650.85	r	17.051	0.014	LCO
60652.23	r	17.137	0.036	REM
60654.13	r	17.329	0.121	REM
60656.07	r	17.594	0.058	REM
60656.46	r	17.514	0.03	LCO
60658.14	r	17.785	0.112	REM
60658.46	r	17.682	0.028	LCO
60660.46	r	18.109	0.039	LCO
60661.04	r	18.106	0.062	REM
60662.92	r	18.461	0.042	LCO
60663.12	r	18.57	0.08	REM
60664.46	r	18.818	0.042	LCO
60665.14	r	18.922	0.067	REM
60666.81	r	19.232	0.063	LCO
60667.16	r	19.397	0.061	REM
60668.47	r	19.745	0.113	LCO
60670.75	r	20.434	0.071	AFOSC
60671.04	r	20.269	0.079	REM
60672.13	r	20.604	0.136	REM
60672.46	r	20.716	0.187	LCO
60673.15	r	20.823	0.244	REM
60674.13	r	21.016	0.253	REM
60675.06	r	20.867	0.204	LCO
60676.06	r	21.331	0.227	REM
60677.04	r	20.87	0.271	LCO
60680.09	r	21.785	0.311	REM
60684.12	r	20.129	0.14	REM
57710.38	i	>21.008	-	PS1
57971.58	i	>22.599	-	PS1
58063.39	i	>22.614	-	PS1
58719.55	i	>22.659	-	PS1
59101.6	i	>22.458	-	PS1
59511.41	i	>21.654	-	PS1
59838.48	i	>22.060	-	PS1
60220.55	i	>21.469	-	PS1
60630.34	i	>19.873	-	PS1
60642.98	i	16.936	0.017	LCO
60643.09	i	16.912	0.035	REM
60643.74	i	16.891	0.027	67/91,Moravian-DIF
60644.11	i	16.869	0.083	REM
60644.81	i	16.873	0.014	LCO
60645.22	i	16.873	0.036	REM
60646.23	i	16.905	0.113	REM
60646.79	i	16.88	0.015	LCO
60648.03	i	16.977	0.029	REM
60649.08	i	17.049	0.014	LCO
60650.21	i	17.078	0.089	REM
60650.85	i	17.12	0.015	LCO
60652.23	i	17.188	0.103	REM
60654.13	i	17.287	0.064	REM
60656.07	i	17.447	0.115	REM
60656.46	i	17.514	0.028	LCO
60658.14	i	17.638	0.09	REM
60658.46	i	17.68	0.034	LCO

Table A2 continued from previous page

MJD	Band	mag	err	marker
60660.46	i	17.855	0.033	LCO
60661.04	i	17.951	0.04	REM
60662.92	i	18.267	0.053	LCO
60663.12	i	18.362	0.133	REM
60664.46	i	18.461	0.038	LCO
60665.14	i	18.603	0.141	REM
60666.81	i	18.966	0.075	LCO
60667.16	i	18.985	0.088	REM
60668.47	i	19.583	0.099	LCO
60670.74	i	20.206	0.053	AFOSC
60671.04	i	19.92	0.133	REM
60672.13	i	20.086	0.18	REM
60672.47	i	20.391	0.161	LCO
60673.15	i	20.227	0.205	REM
60674.13	i	>20.282	-	REM
60675.06	i	20.345	0.155	LCO
60676.06	i	20.55	0.181	REM
60677.04	i	20.536	0.241	LCO
60680.09	i	20.918	0.281	REM
60684.12	i	>19.880	-	REM
60642.82	z	17.083	0.038	TTT
60642.98	z	17.103	0.023	LCO
60642.99	z	16.993	0.033	TTT
60643.09	z	17.013	0.145	REM
60643.96	z	17.055	0.033	TTT
60644.11	z	16.98	0.276	REM
60644.81	z	16.964	0.024	LCO
60644.82	z	17.002	0.030	TTT
60645.01	z	16.932	0.040	TTT
60645.22	z	16.988	0.28	REM
60646.23	z	17.024	0.094	REM
60646.79	z	16.992	0.021	LCO
60646.82	z	17.005	0.195	TTT
60646.99	z	17.058	0.038	TTT
60647.82	z	17.040	0.036	TTT
60647.99	z	16.978	0.035	TTT
60648.03	z	17.086	0.17	REM
60649.08	z	17.091	0.021	LCO
60650.21	z	17.153	0.369	REM
60650.85	z	17.178	0.018	LCO
60652.23	z	17.23	0.31	REM
60654.13	z	17.356	0.171	REM
60656.07	z	17.505	0.16	REM
60656.46	z	17.508	0.033	LCO
60658.14	z	17.713	0.282	REM
60658.46	z	17.615	0.054	LCO
60660.46	z	17.87	0.052	LCO
60661.04	z	18.022	0.259	REM
60662.92	z	18.205	0.056	LCO
60663.12	z	18.261	0.158	REM
60664.46	z	18.357	0.049	LCO
60665.14	z	18.51	0.298	REM
60666.81	z	18.808	0.133	LCO
60667.16	z	18.806	0.48	REM
60668.48	z	19.224	0.117	LCO
60670.74	z	19.788	0.089	AFOSC
60671.04	z	>19.383	-	REM
60672.13	z	>19.273	-	REM
60672.47	z	19.957	0.209	LCO
60673.15	z	>19.127	-	REM

Table A2 continued from previous page

MJD	Band	mag	err	marker
60674.13	z	>19.122	-	REM
60675.06	z	19.842	0.18	LCO
60676.06	z	>19.333	-	REM
60677.04	z	19.987	0.262	LCO
60680.09	z	>19.488	-	REM
60684.12	z	>18.748	-	REM
58345.6	w	>22.788	-	PS1
58351.59	w	>22.488	-	PS1
58489.24	w	>22.189	-	PS1
58733.54	w	>22.372	-	PS1
58751.49	w	>23.444	-	PS1
58752.5	w	>23.212	-	PS1
58813.3	w	>23.675	-	PS1
59105.52	w	>23.576	-	PS1
59140.45	w	>23.527	-	PS1
59195.28	w	>22.591	-	PS1
59218.24	w	>23.225	-	PS1
59222.29	w	>22.081	-	PS1
59465.56	w	>23.300	-	PS1
59486.55	w	>22.440	-	PS1
59490.4	w	>23.236	-	PS1
59500.38	w	>22.242	-	PS1
59516.32	w	>23.048	-	PS1
59527.28	w	>22.359	-	PS1
59543.29	w	>23.391	-	PS1
59810.61	w	>23.168	-	PS1
59822.54	w	>23.647	-	PS1
59827.53	w	>23.037	-	PS1
59850.49	w	>23.315	-	PS1
59870.38	w	>23.046	-	PS1
59907.37	w	>22.642	-	PS1
60175.59	w	>22.886	-	PS2
60208.51	w	>22.024	-	PS1
60223.46	w	>22.438	-	PS1
60227.44	w	>22.674	-	PS2
60232.39	w	>22.321	-	PS2
60235.39	w	>22.977	-	PS1
60238.4	w	>22.771	-	PS2
60256.34	w	>22.888	-	PS1
60259.38	w	>22.408	-	PS1
60264.33	w	>22.434	-	PS1
60283.31	w	>23.031	-	PS2
60290.23	w	>22.820	-	PS1
60559.55	w	>22.170	-	PS2
60563.51	w	>23.368	-	PS1
60564.55	w	>23.306	-	PS1
60581.5	w	>22.857	-	PS2
60588.42	w	>22.261	-	PS1
60592.45	w	>22.380	-	PS2
60605.39	w	>22.555	-	PS2
60635.33	w	19.876	0.028	PS1
60641.32	w	17.096	0.004	PS1
60642.98	w	16.877	0.1	NOT
60647.29	w	16.768	0.002	PS2
60616.07	L	>18.000	-	GOTO-L
60636.92	L	18.340	0.110	GOTO-L
60636.92	L	18.335	0.108	GOTO-L
60640.48	L	17.160	0.019	GOTO-L
60640.48	L	17.277	0.043	GOTO-L
60656.54	L	17.605	0.087	GOTO-L

Table A2 continued from previous page

MJD	Band	mag	err	marker
60656.54	L	17.684	0.069	GOTO-L
60664.86	L	18.721	0.191	GOTO-L
60633.04	q	>21.030	-	BlackGem
60640.04	q	17.270	0.020	BlackGem
60608.99	cyan	>20.856	-	ATLAS
60614.40	cyan	>20.695	-	ATLAS
60616.99	cyan	>18.787	-	ATLAS
60635.12	cyan	>20.717	-	ATLAS
60636.34	cyan	18.669	0.050	ATLAS
60639.11	cyan	17.430	0.016	ATLAS
60640.35	cyan	17.178	0.015	ATLAS
60642.98	cyan	16.897	0.100	NOT (spectrum)
60643.12	cyan	16.778	0.011	ATLAS
60644.32	cyan	16.813	0.054	ATLAS
60647.09	cyan	16.836	0.012	ATLAS
60672.80	cyan	20.465	0.251	ATLAS
60696.26	cyan	>20.740	-	ATLAS
60704.28	cyan	>19.673	-	ATLAS
60602.47	orange	>20.366	-	ATLAS
60603.24	orange	>19.912	-	ATLAS
60604.41	orange	>20.466	-	ATLAS
60607.17	orange	>20.613	-	ATLAS
60611.19	orange	>20.307	-	ATLAS
60612.51	orange	>19.998	-	ATLAS
60615.18	orange	>20.695	-	ATLAS
60616.40	orange	>20.655	-	ATLAS
60618.27	orange	>20.835	-	ATLAS
60619.14	orange	>20.634	-	ATLAS
60620.90	orange	>20.556	-	ATLAS
60623.14	orange	>20.520	-	ATLAS
60624.53	orange	>20.307	-	ATLAS
60630.46	orange	>19.749	-	ATLAS
60631.15	orange	>20.020	-	ATLAS
60632.89	orange	>20.384	-	ATLAS
60634.35	orange	>20.537	-	ATLAS
60636.85	orange	18.265	0.044	ATLAS
60638.34	orange	17.740	0.016	ATLAS
60642.98	orange	16.923	0.100	NOT (spectrum)
60644.83	orange	16.847	0.015	ATLAS
60648.81	orange	16.983	0.022	ATLAS
60650.29	orange	17.083	0.015	ATLAS
60651.09	orange	16.829	0.018	ATLAS
60652.57	orange	17.205	0.017	ATLAS
60656.42	orange	17.680	0.161	ATLAS
60658.32	orange	17.823	0.045	ATLAS
60659.13	orange	17.791	0.083	ATLAS
60660.58	orange	17.964	0.036	ATLAS
60663.08	orange	18.381	0.051	ATLAS
60664.58	orange	18.621	0.063	ATLAS
60666.30	orange	18.982	0.071	ATLAS
60667.05	orange	19.099	0.120	ATLAS
60668.29	orange	19.686	0.154	ATLAS
60671.05	orange	>20.257	-	ATLAS
60672.30	orange	20.391	0.269	ATLAS
60674.27	orange	20.544	0.354	ATLAS
60678.26	orange	20.496	0.307	ATLAS
60679.04	orange	>19.861	-	ATLAS
60680.26	orange	20.675	0.358	ATLAS
60682.24	orange	>20.126	-	ATLAS
60684.26	orange	>20.433	-	ATLAS

Table A2 continued from previous page

MJD	Band	mag	err	marker
60687.11	orange	>19.309	-	ATLAS
60688.80	orange	>19.684	-	ATLAS
60690.29	orange	>19.915	-	ATLAS
60692.82	orange	>20.235	-	ATLAS
60694.27	orange	>20.433	-	ATLAS
60643.09	J	16.668	0.155	REMIR
60644.22	J	16.609	0.367	REMIR
60646.23	J	16.579	0.168	REMIR
60648.05	J	16.603	0.095	REMIR
60650.24	J	16.681	0.139	REMIR
60654.14	J	16.809	0.100	REMIR
60656.15	J	16.882	0.158	REMIR
60658.15	J	16.945	0.139	REMIR
60661.06	J	17.339	0.365	REMIR
60643.10	H	16.327	0.212	REMIR
60644.23	H	16.180	0.192	REMIR
60646.24	H	16.120	0.118	REMIR
60648.05	H	16.128	0.105	REMIR
60650.25	H	16.163	0.258	REMIR
60654.15	H	16.250	0.142	REMIR
60656.15	H	16.312	0.146	REMIR
60658.16	H	16.353	0.179	REMIR
60661.06	H	16.548	0.177	REMIR
60643.11	K	16.057	0.428	REMIR
60644.12	K	15.917	0.273	REMIR
60645.23	K	15.849	0.371	REMIR
60646.26	K	15.778	0.307	REMIR
60648.03	K	15.813	0.466	REMIR
60650.23	K	15.851	0.374	REMIR
60652.24	K	15.891	0.477	REMIR
60656.08	K	15.951	0.458	REMIR
60658.22	K	15.979	0.441	REMIR
60661.05	K	16.108	0.348	REMIR
60641.84	UVM2	16.650	0.080	UVOT
60643.67	UVM2	16.530	0.050	UVOT
60645.70	UVM2	16.640	0.050	UVOT
60650.99	UVM2	18.060	0.090	UVOT
60656.42	UVM2	>18.970	-	UVOT
60659.23	UVM2	>19.010	-	UVOT
60641.84	UVW2	17.010	0.080	UVOT
60643.67	UVW2	16.860	0.060	UVOT
60645.70	UVW2	17.060	0.060	UVOT
60650.99	UVW2	18.250	0.110	UVOT
60656.42	UVW2	>19.540	-	UVOT
60659.23	UVW2	>19.570	-	UVOT
60641.84	UVW1	16.430	0.100	UVOT
60643.67	UVW1	16.120	0.090	UVOT
60645.70	UVW1	16.350	0.090	UVOT
60650.99	UVW1	17.360	0.120	UVOT
60656.42	UVW1	18.670	0.210	UVOT
60659.23	UVW1	>18.730	-	UVOT